Timing Studies for the H_iSCORE Detector

Diplomarbeit

vorgelegt von
Michael Büker

Gutachter:
Prof. Dr. Dieter Horns
Prof. Dr. Erika Garutti

Institut für Experimentalphysik
Universität Hamburg

Dezember 2012

Universität Hamburg
DER FORSCHUNG | DER LEHRE | DER BILDUNG

Abstract: The H_iSCORE experiment is set to be a large-area cosmic gamma-ray observatory, designed to detect ultra-high energy gamma-rays with a large number of non-imaging atmospheric Cherenkov light detector stations. For gamma/hadron separation and angular resolution, it relies on precise timing on the order of 1 ns or less. The DRS4 Evaluation Board is a data acquisition device with sampling rates of several GHz. It has been chosen for prototyping H_iSCORE and was investigated for timing accuracy. Normally distributed signal arrival time differences between the different input channels of the device were found. Their magnitudes and distribution spreads were observed to be on the order of 10 to 100 ps. Furthermore, a readout frequency of 525 events per second was achieved over the device's USB connection, which is close to the theoretical limit. Finally, an analog time-tagging system integrated with the detector stations' data flow was drafted. Simulations show it to be viable, but dedicated hardware development will be necessary for an implementation.

Zusammenfassung: Das H_iSCORE-Experiment soll ein großflächiges Observatorium für kosmische Gammastrahlen werden, das ultra-hochenergetische Gammastrahlen mit einer großen Zahl nicht-abbildender Detektorstationen für atmosphärisches Cherenkovlicht misst. Für die Unterscheidung von primären Gammastrahlen und Hadronen sowie für eine gute Winkelauflösung ist es auf präzise Zeitinformationen in der Größenordnung von 1 ns oder weniger angewiesen. Das DRS4 Evaluation Board ist ein Datennahmegerät mit Ausleserate von einigen GHz. Es ist für den Einsatz im H_iSCORE-Prototypen ausgewählt worden und wurde auf Zeitgenauigkeit untersucht. Normalverteilte Zeitunterschiede in der Ankunft der Signale zwischen den verschiedenen Eingangskanälen des Geräts wurden entdeckt. Ihr Betrag und die Breite ihrer Verteilung wurden in der Größenordnung von 10 bis 100 ps gemessen. Weiterhin wurde eine Auslesefrequenz von 525 Ereignissen pro Sekunde über die USB-Verbindung des Geräts erreicht, was nahe der theoretischen Obergrenze liegt. Zuletzt wurde ein analoges Zeitstempel-System entworfen, das im Datenfluss der Detektorstationen integriert sein soll. Simulationen zeigen seine Funktionstüchtigkeit, aber gezielte Hardwareentwicklung wird für eine Implementation notwendig sein.

Für Uroma.

„Lern Junge, immer lern [...] Was'd im Kopp hast kann Dir kejner wegnehm!“
Julianna Kutzner (1911—2008)

Contents

V. Appendix

Part I.
Introduction

Look at me still talking
when there's Science to do.

—GLaDOS

---

from *Portal*,
Valve Corporation (2007)

1. Cosmic rays and air showers

At the beginning of the 20$^{\text{th}}$ century, many physicists were concerned with the investigation of the newly discovered phenomenon known as radioactivity. Observations of charged electroscopes—which are basically large capacitors with mechanical components to indicate the magnitude of their charge, see Fig. 1 for a contemporary device—had shown that they would discharge over time, independent of their material or construction. With earlier experiments indicating that the rate of discharge would decrease both when air pressure around the electroscope was reduced and when it was shielded from the outside by metal, the effect was ascribed to external "penetrating radiation", namely the action of charged particles created in radioactive processes [5].

Radioactive material in the earth's crust was by far the most popular explanation for the origin of this radiation. Two competing theories, the presence of radioactive material dispersed in the atmosphere and an extra-terrestrial origin of the radiation, were also on the table from the beginning, but were rather unpopular and therefore scarcely discussed. They gained traction only when experimental results challenged the plausibility of the earth's crust being the *sole* source of radiation:

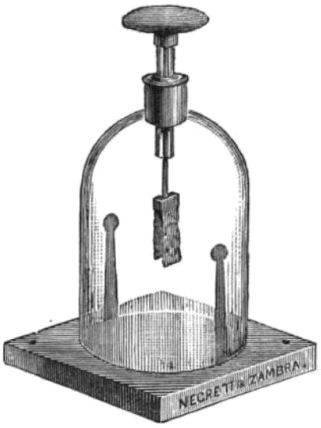

Figure 1: An illustration of an electroscope contemporary to the discovery of cosmic rays. Image from [30].

In 1909, German physicist and priest Theodor Wulf measured the ionization at an elevation of 300 m at the top of the Eiffel tower in Paris, the world's tallest edifice at the time. He found that the decrease in ionization between ground level and the elevation of the Eiffel tower was much smaller than expected—so small, in fact, that it seemed incompatible with the dominant terrestrial radiation model. Yet, Wulf himself did not call that model into question at the time [50].

In 1911, Italian geophysicist Domenico Pacini submerged an electroscope several meters deep in the Mediterranean sea, having purposefully selected a location with a large amount of water between his devices and both the sea bed and the shore. He found that ionization decreased significantly when the device was submerged as opposed to control measurements above the surface of the water. Using the already well-understood radiative attenuation properties of water, he concluded that radioactivity of the soil could not explain the observations [33]. His summary of the observations was [33, translation from [34]]:

> [...] that a sizable cause of ionization exists in the atmosphere, originating from penetrating radiation, independent of the direct action of radioactive substances in the soil.

From 1910 on, physicist Albert Gockel conducted experiments in Switzerland in which he measured atmospheric ionization at high altitudes in a free balloon. He also failed to find the expected decrease in ionization and confirmed Pacini's conclusions [15, translation from [5]]:

> [...] that a non-negligible part of the penetrating radiation is independent of the direct action of the radioactive substances in the uppermost layers of the earth.

In spite of all these findings, a non-terrestrial origin of the pervasive ionization did not gain widespread acceptance until Austrian physicist Victor Hess undertook a long series of free balloon flights over Austria and Germany with different types of electroscopes. Crucially, and in contrast to Pacini's submersion experiments, Wulf's measurements at low altitudes and Gockel's lone balloon flight, he conducted several series of measurements over many hours with different instruments and under varying external conditions [19].

Hess found only a slight decrease in ionization at altitudes up to 1000 m, but a drastic rise above 3000 m. The high altitudes and the routes of his flights allowed him to argue meteorologically and exclude the possibility of radioactive materials released from the ground and dispersed in the atmosphere being responsible for the ionization he observed. Thus, he concluded [19, p. 1090, own translation]:

> [...] that a radiation of very high penetrativeness enters our atmosphere from above, [...]

Hess' balloon flights took place at different times of day and night, and once even during a partial solar eclipse over Austria. Since he found no significant variation in the ionization under those circumstances, he ruled out the sun as the principal source of the ionizing radiation. He coined the term "Höhenstrahlung" (*radiation at high altitude*) for his discovery [5].

After research had been severely impeded during the World War I, Robert Millikan in the 1920s prominently conducted experiments aimed at uncovering the nature of the ionizing radiation which he had dubbed *cosmic rays*. After a series of both high-altitude and water submersion experiments, he came to vehemently defend his theory that cosmic radiation was made up of γ-rays created in the cosmic recombination of helium atoms. This view was revised only after many large-scale experiments, conducted in the 1930s by Arthur Holly Compton and others, confirmed that cosmic radiation was subject to geomagnetic effects. Since only charged particles, not photons, would be susceptible to the earth's magnetic field, it was concluded that cosmic rays were indeed made up mostly of charged particles. Longitudinal dependencies even pointed to positively charged particles as their main component, but this was not confirmed until protons were identified as such in the 1940s [5].

1.1. The cosmic ray spectrum

Figure 2 on the following page shows a famous representation (the *Swordy plot*) of the flux of cosmic rays arriving at earth. Many different experiments have been in very good agreement over the basic shape of this spectrum for decades. In the double-logarithmic representation, it is obvious that the energy-flux relation follows an inverse power law with the *spectral index* Γ:

$$\frac{\mathrm{d}N}{\mathrm{d}E} \propto E^{-\Gamma}.$$

For some reason, the most prominent features of this cosmic ray spectrum are described in terms of the anatomical features of a human leg as can be recognized—with some imagination—in the Swordy plot.

For energies between roughly 10^{10} eV and 10^{15} eV, Γ has a value of 2.7. In a feature called the *knee* at about 10^{15} eV, the slope steepens (the spectrum is getting *softer*) to $\Gamma = 3.1$. Another slight softening occurs at 10^{18} eV, recognized by some as the *second knee*. Another prominent feature called the *ankle* is seen above 10^{18} eV, where the spectrum hardens drastically. The apparent breaking off of the spectrum at about 10^{20} eV is a feature called the *GZK cutoff*, explained in more detail on page 12 [3].

It should be noted that this popular representation of the spectrum, due to its double-logarithmic nature, is suggestive of the false conclusion that a large part of the spectrum is populated by high-energy particles. But in fact, the decrease in cosmic ray particle flux with energy is dramatic: thousands of particles arrive in one square meter per second at GeV energies, where at knee energies of several PeV, only one particle per square meter per year is expected. At ankle energies, the appropriate units are square kilometers and centuries.

The origin and the composition of cosmic rays have since their discovery been the subject of much research and speculation, which is still ongoing. The most striking property of the cosmic ray spectrum at all energies is its *nonthermal* shape (as opposed to a *thermal* spectrum, which would follow a Planck distribution around some definite temperature), meaning that acceleration processes beyond thermal emission must be at work.

Sub-knee energies. For cosmic ray particles at energies below the knee, a widely accepted theory is that charged particles are accelerated to energies up to several 10^{15} eV in a process known as *Fermi acceleration*, a magnetohydrodynamic effect at rapidly expanding shock fronts, as occur in supernova remnants [3]. In the case of the ancient but well-documented local[†] supernova SN 1006, it has been conclusively established that its remnant is indeed host to nonthermal acceleration phenomena. Its large angular diameter has allowed spatially resolved examinations of its electromagnetic spectrum. Over the last ten years, observations have shown that while thermal emission dominates in the center of the remnant, the shock front at its rim shows X-ray emissions

[†]Hereinafter, *local* shall mean *in our own Galaxy.*

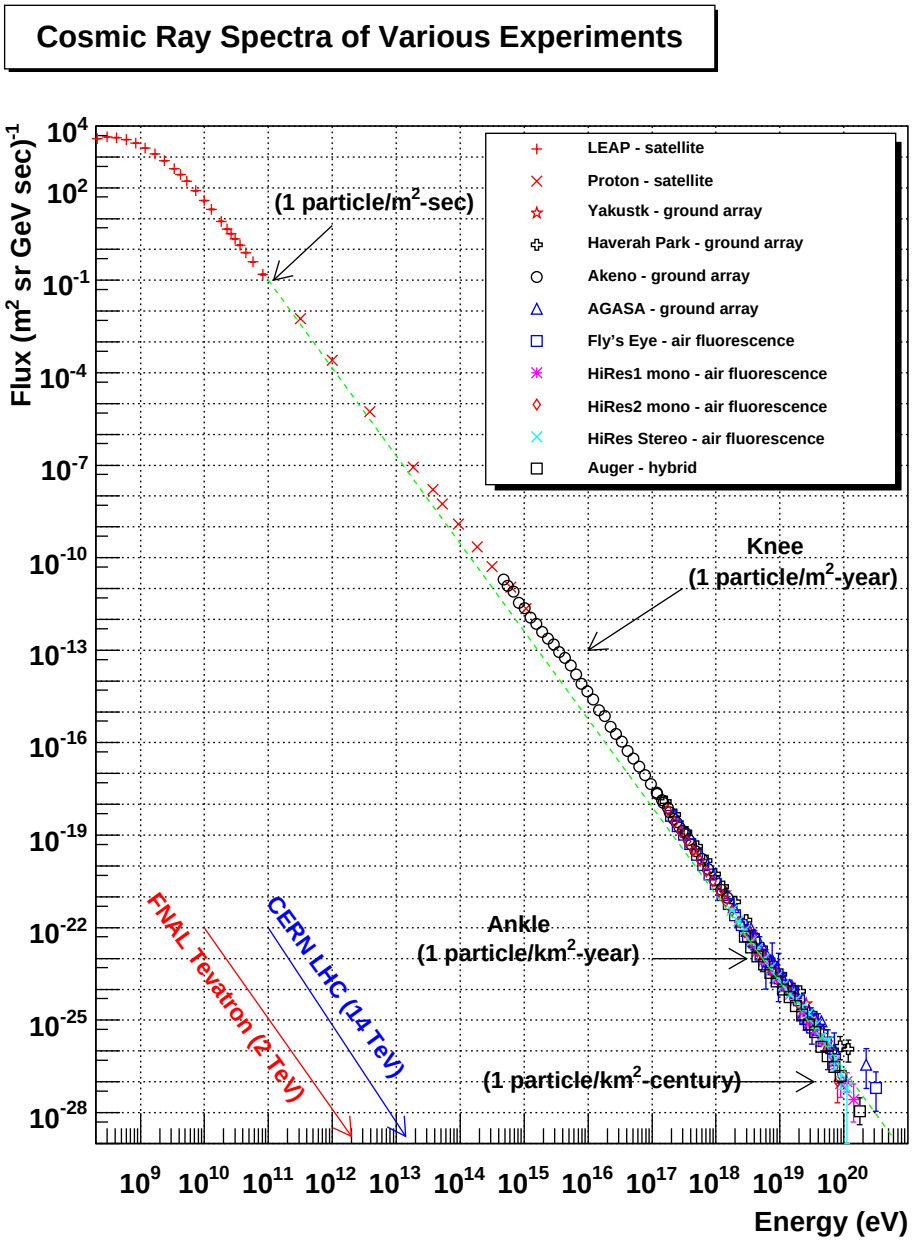

Figure 2: A plot of cosmic ray energy vs. flux at earth, as measured by several space- and ground-based experiments over several decades. This particular representation is known as the *Swordy Plot*, after astrophysicist Simon Swordy (1954–2010). Image from [18]. For a more detailed view of the ankle region, see Fig. 3 on the next page.

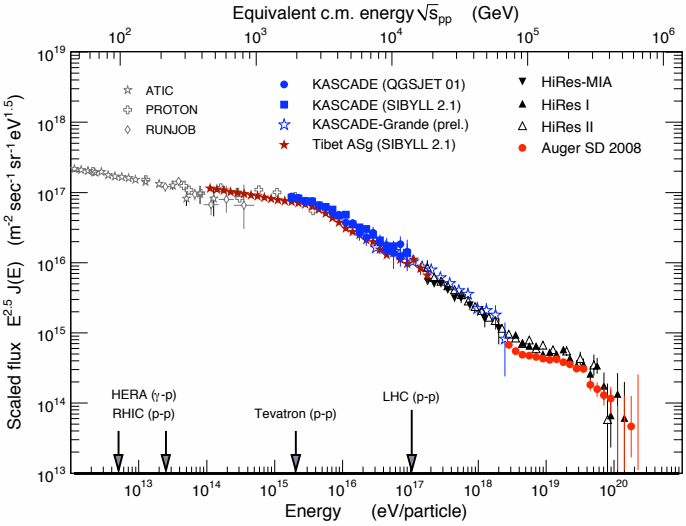

Figure 3: A plot detailing the cosmic ray spectrum at TeV energies and above, as measured by several space- and ground-based experiments over several decades. For comparison, the center-of-mass energy of some of the most powerful human-made collider experiments is indicated by arrows on the bottom horizontal axis. Note the clearly visible breaks at ankle and GZK cutoff energies. Image from [3].

compatible with the synchrotron radiation of accelerated charged particles [28, 2] as well as γ-ray emissions expected from accompanying inverse Compton scattering [21].

These indirect observations of nonthermal processes are compatible with the idea that supernova remnants are indeed the "local cosmic accelerators" responsible for the cosmic ray spectrum up to knee energies. Furthermore, estimates show that the local rate of supernova occurrences is indeed sufficient to maintain the energy density of galactic cosmic rays as observed on earth [3].

The composition of cosmic rays can best be studied at sub-knee energies, because high fluxes allow for the direct detection and identification of different nuclei outside the atmosphere (see the next section). As is obvious in Fig. 4 on the following page, nuclear abundances of most of the lighter elements are much higher in cosmic rays than in our solar system, sometimes by many orders of magnitude. This is ascribed to spallation processes, in which heavier elements in cosmic rays break up into lighter nuclei in cosmic interactions [3].

The knee and beyond. Possible causes for the knee itself are still the subject of discussion. The two main theories are that it either marks the maximum energy attainable in supernova remnant acceleration, or that particles at trans-knee energies are no longer magnetically bound to the Galactic disk and escape it, leading to a softening of the spectrum from a local point of view.

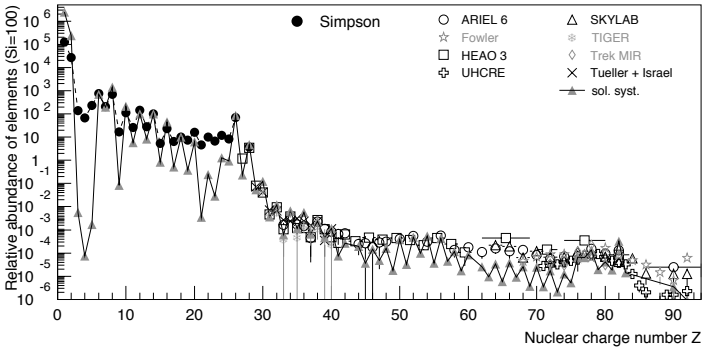

Figure 4: Relative abundances of nuclei in cosmic rays by their charge number Z in comparison to the overall abundance of elements in the solar System. Note the logarithmic scale on the vertical axis, which is normalized to a relative abundance of 100 for $Z = 14$ (silicon). Image from [3].

As for the cosmic rays observed above knee energies (also known as *ultra-high energy cosmic rays* or UHECR), there are only a few currently known likely candidates for their origin, including active galactic nuclei (AGN) and gamma-ray bursts (GRBs) [3]. An important constraint on such objects is that the product of their expanse and their magnetic field has to be large for the particles to be magnetically bound long enough to be accelerated to the energies observed [16].

Ankle and cutoff. Whether or not cosmic rays of trans-knee energies could be of local origin or not is still subject to debate, with some theories even pointing to new particle physics like dark matter interactions rather than astronomical objects [3]. In any case, at ankle energies of about $10^{18.5}$ eV, a low-flux, hard-spectrum component appears to take over the cosmic ray spectrum, which is widely believed to be of extra-galactic origin for lack of any conceivable kind of local source.

For the distance of such UHECR sources, there is a theoretical constraint: the *GZK cutoff*[†]. It states that cosmic rays of energies of about $5 \cdot 10^{19}$ eV and more are highly likely to undergo *pion photoproduction*, an electromagnetic interaction with the cosmic microwave background that produces Delta baryons, which quickly decay into pions [51]. This effect is expected to suppress extra-galactic UHECR and make the universe opaque to them at distances of more than a few hundred Mpc. Therefore, only objects within this distance (the *GZK sphere*) are considered possible UHECR source candidates at the moment.

The Centaurus A galaxy, about 3 to 5 Mpc from our Galaxy, is considered a likely candidate. The Pierre Auger Observatory has claimed a significant correlation between UHECR arrival directions and the direction of Cen A [35], and the H.E.S.S. experiment

[†]Named after astrophysicists K. Greisen, V. Zatsepin and G. Kuzmin.

has observed γ-ray emissions of $\gtrsim 10^{11}$ eV from it [20]. Yet, Auger's observations are not yet a significant discovery, and it is uncertain whetheher there will ever be one. Despite their very large impulses, UHECR are deflected in both the Galactic and the intergalactic magnetic field, and very little is known about the latter.

Definite results on the anisotropy of ankle-energy UHECR at earth, if there is any, will be an important piece of the puzzle of the origin and propagation of cosmic rays, but their extremely low flux greatly complicates measurements.

Gamma-rays. Charged particles dominate the cosmic ray spectrum observed at earth both in abundance and in energy. Still, γ-rays are an invaluable source of insight into cosmic accelerators, as they propagate through the universe undisturbed by magnetic fields. A seemingly isotropic flux of cosmic ray particles may be resolved to distinct sources by observing γ-rays originating from them. Even further insight into cosmic accelerators, once identified, can be gained by observing their γ-ray spectra. Non-thermal emissions from synchrotron or bremsstrahlung radiation as well as inverse Compton scattering, annihilation or neutral particle decays can provide valuable clues about acceleration processes [3]. See section 2.2 on page 18 for details.

The same is true for neutrinos, with the additional benefit of identifying hadronic processes in their source regions. They are, however, extremely difficult to detect directly, and despite great efforts, only upper bounds have been found for the flux of cosmic neutrino sources [25].

1.2. Extensive air showers

As described in the previous section, cosmic ray flux decreases dramatically with higher cosmic ray energies. This affects the ways in which they are detected: At low energies, direct measurements with satellite-based detectors outside the atmosphere are the preferred experimental method. There, cosmic rays are not disturbed by collisions with the constituent particles of the atmosphere and are less affected by the earth's magnetic field. Low-energy cosmic rays that enter the atmosphere lose their energy in collisions with atmospheric molecules, but these collisions are too weak to cause any observable effect on the ground.

At higher energies, the picture is reversed: The cosmic ray flux becomes too small for typical space-based detectors (with effective areas on the order of a few square meters) to realistically observe any useful number of events. But once the particles do enter the atmosphere, they cause extensive air showers that can be observed with ground-based detectors. The energy above which air showers are seen on the ground is about 10^{11} eV, while direct-detection experiments are feasible up to 10^{14} eV. This means there is an energy range of a few orders of magnitude in which both experimental methods are viable. For γ-rays, there is almost no such overlap, with direct detection failing and extensive air showers becoming significant between 10^{10} eV and 10^{11} eV.

Extensive air showers triggered by cosmic ray particles and γ-rays share many characteristics, but they differ in some aspects which are crucial to their detection and

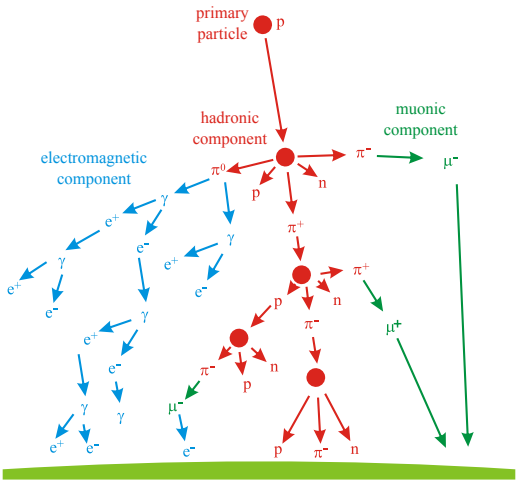

Figure 5: A schematic illustration of the development of an extensive air shower and the most common interactions in their development. Image modified from [32].

investigation. The distinction of primary particles from the properties of an air shower is called *gamma/hadron separation*, which is explained in more detail below.

Air showers develop after the primary incident particle's collision with an air molecule triggers a cascade of collisions and reactions in which the number of particles involved increases dramatically. The resulting cloud of particles has the approximate shape of a disc perpendicular to the primary particle's flight direction and reaches the ground roughly 100 μs after the initial collision.

Such extensive air showers are triggered by primary γ-rays and hadronic particles. Incident electrons and γ-rays go through a series of bremsstrahlung emissions and pair production processes that greatly increase the number of particles, while hadronic primary particles such as protons or heavier nuclei cause an air shower that is mostly driven by pions created in collisions with nuclei in the air.

Hadronic showers always have an electromagnetic (EM) component due to neutral pion decays giving off high-energy γ-rays. Because this process usually occurs shortly after the primary interaction, the EM component in a hadronic shower is very similar in size and nature to a cascade caused by a leptonic or γ-ray primary [44, 16]. Conversely, an EM cascade also has a hadronic component, caused mainly by photon-nucleon interactions between γ-rays in the cascade and air molecules leading to pion creation (a process also called *photopion production*), but these hadronic components of EM cascades are much weaker than original hadronic showers [38, 16].

Both types of events also have a *muonic* component, fed mostly by charged pion decays. However, the muons do not contribute significantly to the expansion of the cascade due to their long lifetime and small interaction cross sections. These muons make for a constant and pervasive isotropic background of charged particles at the ground.

Figure 5 on the preceding page gives a schematic overview of the different components of air showers, and Fig. 6 on the next page illustrates differences in the typical shapes of hadronic air showers and EM cascades.

The number of particles in an extensive air shower is dependent on the amount of atmosphere traversed, and therefore the height above the ground. In astroparticle physics, this entity is most commonly given as the *atmospheric depth*, expressed in $\mathrm{g/cm^2}$. It is calculated by integrating over the atmospheric mass density along the path of a particle. For a particle travelling vertically downward into the atmosphere, the atmospheric depth X at height H is:

$$X = -\int_{\infty}^{H} \rho(h)\,\mathrm{d}h,$$

with $\rho(h)$ being the atmospheric density at height h. In realistic simulations, this calculation gets rather complicated, taking into account meteorological conditions and a horizontal component to the particles' path. Generally, the atmospheric depth at ground level: $-\int_{\infty}^{0} \rho(h)\,\mathrm{d}h$ is estimated to be $1\,000\,\mathrm{g/cm^2}$.

With λ the typical *mean free path* of electrons in air[†], a simple approximation of the number of electrons in an electromagnetic cascade at depth X is given by the Gaisser-Hillas profile [12]:

$$N_e(X) = N_{\max}\left(\frac{X - X_1}{X_{\max} - X_1}\right)^{\frac{X_{\max}-X_1}{\lambda}} \cdot \mathrm{e}^{\frac{X_{\max}-X}{\lambda}}.$$

Here, $N_{\max}$ is the maximum number of particles, X_{max} is the depth at which this maximum occurs, and X_1 is the depth of the first interaction. Given the critical energy E_c for electrons in air[‡], $N_{\max}$ and X_{max} can be estimated as [16]:

$$N_{\max} = \frac{E_0}{E_c}, \qquad X_{\max} = \frac{\lambda}{\ln 2} \cdot \ln\left(\frac{E_0}{E_c}\right).$$

Figure 7 on the following page gives an overview of the composition of an extensive air shower triggered by a primary hadron of $10^{19}\,\mathrm{eV}$. Appendix C.2 on page 78 shows such shower profiles for extensive air showers triggered by different types of primary particles. Note how photons and electrons always make up the largest part of the population by far (over $\gtrsim 99\,\%$), both in hadronic showers and EM cascades.

[†] The mean free path is defined as the depth after traversing which only the $\frac{1}{\mathrm{e}}$th part of the particles has *not* undergone any interaction. It is typically given as $70\,\mathrm{g/cm^2}$ for electrons in air.

[‡] The critical energy is defined as the energy below which electrons in air lose more energy in ionization processes than through bremsstrahlung emissions. It is typically given as 84 MeV in air.

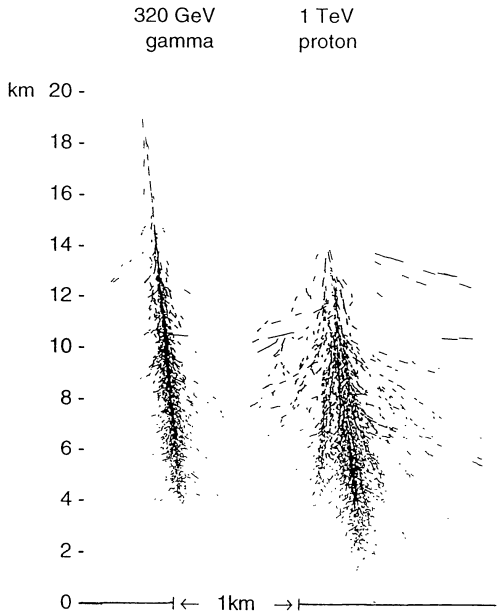

Figure 6: Comparison of the extent of EM and hadronic showers. Note the exaggerated horizontal scale. Image from [23].

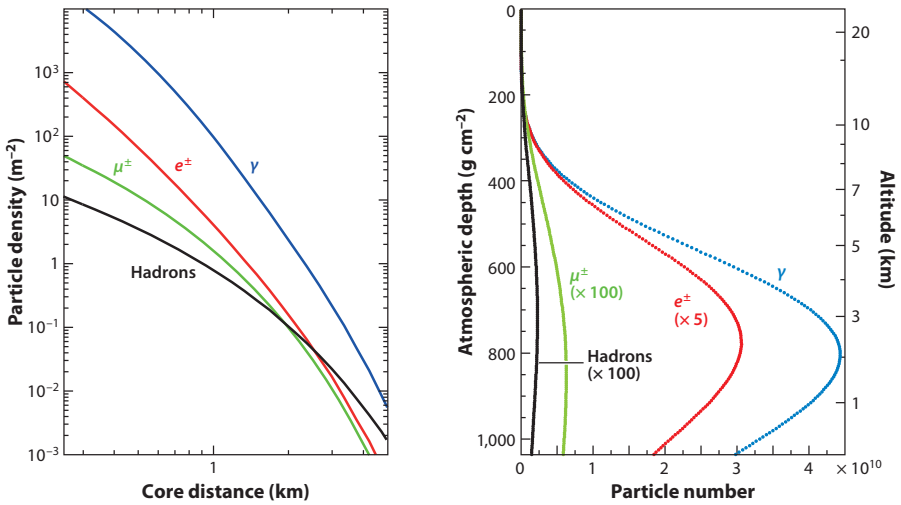

Figure 7: Graphs showing the properties of a simulated extensive air shower initiated by a 10^{19} eV proton. **Right:** Particle number by atmospheric depth/height above ground. **Left:** Particle density by distance from shower core at 870 g/cm^2 (the typical depth of air showers arriving at the Pierre Auger Observatory). Image from [10].

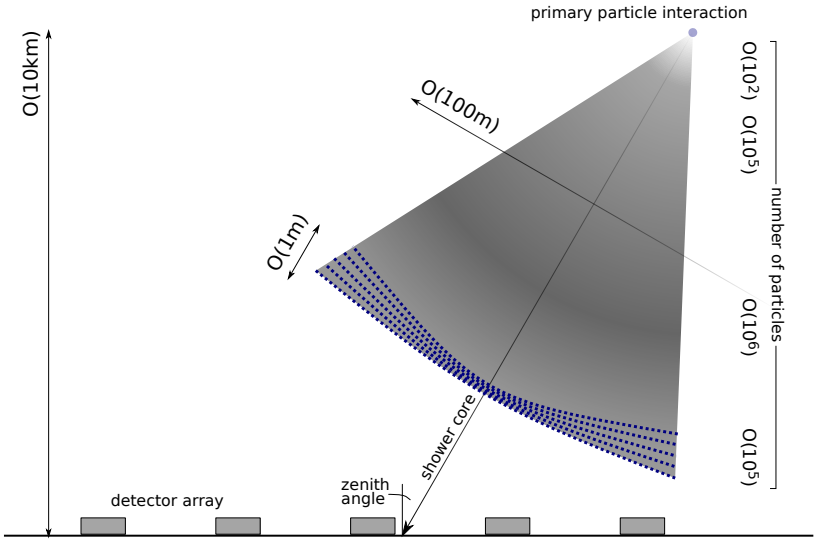

Figure 8: A schematic illustration of the propagation and shape of an extensive air shower. Note that distances are not to scale for better visibility. Image modeled after [47, Fig. 1.5].

2. Cosmic ray and gamma-ray experiments

2.1. Direct particle detection

Commonly, extensive air showers are investigated by spacing out a number of particle detectors over some area and using them to detect the particles of an EAS directly—or, more precisely, those particles of an EAS that reach ground level. However, due to the constant and pervasive muon background that is usually not correlated with single extensive air showers, they continuously register charged particles. In order to identify the actual hadrons, electrons, and photons associated with specific extensive air showers, temporal coincidence between the different detectors is looked for. For this purpose, intricate trigger systems are necessary to separate background noise from real signals.

As illustrated in Fig. 8, the different stations of an array register particles from an extensive air shower at different times, depending on its angle of incidence (*zenith angle*). The larger this angle, the larger the time difference between the first and the last detector to register particles will be.

Conversely, this means that with precise measurements of this time delay, the zenith angle can be reconstructed from the gathered data, provided that enough detector stations contribute signals. From the number of particles registered, or the amount of energy deposited in the detectors, the size of the air shower and therefore the energy

of the primary particle can be reconstructed. Note that for most experiments, even large air showers trigger only a fraction of the stations, depending on their spacing. For H$_i$SCORE, large air showers are expected to trigger on the order of 15 stations, while small events may be reconstructed even if only 2 to 5 stations trigger [16].

Generally though, this method does not provide enough detailed information to distinguish between hadronic air showers and electromagnetic cascades, and are therefore unable to identify the nature of the primary particle. Special muon detectors used in direct detection experiments, as in the KASCADE-Grande experiment, can be an exception from this rule [4]. The following subsection focuses on investigations of secondary EAS emissions for gamma/hadron separation.

2.2. Secondary emissions and gamma-ray observation

A number of processes associated with extensive air showers can provide information about the initiation and development of the EAS. These secondary emissions occur all along the path of the EAS and therefore carry more information than just the particles which reach the ground. They are, in essence, a way to look at the development of the shower after it has passed.

As with direct detection methods, there is a pervasive background against which the actual events have to be filtered out. In the case of air fluorescence and Cherenkov detectors, all visible light contributes to the background, be it from artificial, human-made light sources, the moon or bright planets. Even in moonless nights and in remote, unpopulated areas, the starlight still poses a challenge to triggering and filtering systems for data acquisition. Radio detection is mainly disturbed by a wide variety of human-made radio transmissions for broadcasting or communication.

Another criterion that sets these methods apart from most direct detection experiments is that information can more readily be inferred about the nature of the primary particle – hadron, lepton or photon. Whereas hadronic and leptonic air showers are (for most current experiments) isotropic and not correlated with celestial sources, the reconstructed direction of a γ-ray cascade's primary particle points directly at its source, because photons are not deflected by the galactic or terrestrial magnetic fields. Experiments which are able to identify γ-rays and their original sources are therefore also called *gamma-ray observatories*. γ-ray astronomy has so far been able to identify several sources in the lower TeV energy range, but none so far above 100 TeV (10^{14} eV), let alone PeV.

The distinction between the primary particle types is called *gamma/hadron separation*[†]. It involves complex analysis criteria applied to all available information on an EAS [16, 44]. One of these criteria is the signal's rise time, which is on the order of a few nanoseconds (see Fig. 10 on page 20). Also, as illustrated in Fig. 8 on the preceding page, arrival time differences of the shower front at different stations of an array are significant on the order of a few nanoseconds if the direction of origin of the

[†]Neglecting, as is frequently the case in cosmic ray physics, primary leptons.

primary particle is to be reconstructed with accuracies of a few degrees. Therefore, precise timing is crucial to gamma-ray observatories.

There are several secondary emission processes and measurement methods associated with them. The most important of these are detailed below.

Fluorescence. Delayed light emissions (fluorescence) of air molecules excited by EAS particles can be studied with sensitive light detectors pointed at the sky. Fluorescence detectors such as the Auger Fluorescence Detector [36] primarily investigate UV emissions from nitrogen molecules.

Radio emissions. There are radio signals being emitted from extensive air showers, which are believed to be caused by the terrestrial magnetic field deflecting the charged particles and inducing synchrotron emissions from them. Because the terrestrial magnetic field is rather weak, the synchrotron emission are chiefly in the radio part of the electromagnetic spectrum [6]. Investigations of EAS by these radio emissions is probed by the LOPES detector [11] among others.

Cherenkov radiation. A large part of the particles in an EAS are highly relativistic and satisfy the Cherenkov condition of travelling faster than the speed of light in the atmosphere: $v > c/n_{\text{atmosphere}}$ (see Fig. 9 for an illustration of the geometry of this effect). Sensitive light detectors can observe these short pulses and use them to investigate the cosmic rays and γ-rays that caused the associated EAS.

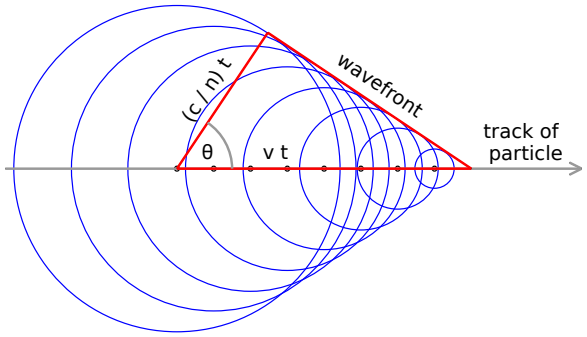

Figure 9: A schematic illustration of Cherenkov radiation being emitted by a relativistic charged particle propagating through a medium. Image from [16].

Imaging Cherenkov detectors operate many photomultiplier tubes (PMTs) in the focal plane of a telescope, and record their output as pixels of a Cherenkov 'photograph' of a portion of the sky with the aim of capturing an image of an EAS' Cherenkov emissions. The main purpose of this setup is to point the array at possible acceleration sources in the sky. The H.E.S.S. telescope array [22] is the largest instrument of this kind to

date, and it has been successful in identifying both Galactic and extragalactic TeV accelerators and even spatially resolving some Galactic sources.

In contrast to imaging Cherenkov detectors, *non-imaging Cherenkov detectors* have a very large field of view ($\sim 1\,\mathrm{sr}$). Instead of using many PMTs for one telescope that resolves a portion of the sky, the telescopes (commonly called *stations*) of non-imaging Cherenkov detectors each comprise only one or a few PMTs with a large field of view. This allows for the construction of arrays with many stations, and thus with a very large effective area (on the order of km^2). Since there is no imagery available for event reconstruction, both gamma/hadron separation and angular resolution depend chiefly on a high time resolution and precise timing synchronization between stations (see Fig. 14 on page 24). The H_iSCORE experiment aims to be the largest detector of this kind, enabling the detection of extremely low-flux (on the order of 1 event per steradian and year) γ-rays in the multi-TeV energy range and identifying the first cosmic PeV accelerators (or *PeVatrons*).

Note that optical Cherenkov detection methods for secondary air shower emissions are not to be confused with *water* Cherenkov detectors, which are used for direct particle detection. They use water as a medium to invoke and detect Cherenkov radiation from relativistic particles. Some of these experiments can be sensitive enough to achieve gamma/hadron separation, such as the past MILAGRO detector and its successor, the HAWC experiment [26].

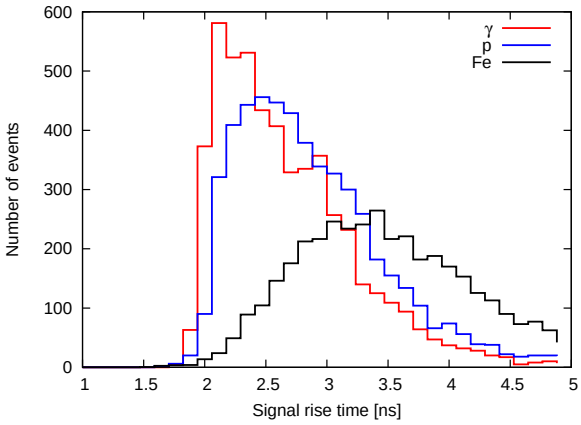

Figure 10: Signal rise time distributions for the Cherenkov emissions of extensive air showers caused by different types of primary particles, simulated with energies between $10^{14}\,\mathrm{eV}$ and $10^{15}\,\mathrm{eV}$. Note the very short time scale on the horizontal axis. Image and simulation from [16].

2.3. The H$_i$SCORE experiment

The name of the H$_i$SCORE experiment stands for "Hundred $\cdot$ i Square kilometer Cosmic Ray ORigin Explorer". It hints at the key principles of the detector: A very large effective area, and the aim of investigating cosmic accelerators.

The H$_i$SCORE detector's chief goal is to observe cosmic ray accelerators of 1 PeV (10^{15} eV) and higher energies—also called *PeVatrons*—by extending current γ-ray observation capabilities to higher energies and detecting γ-rays in the ultra-high energy range of $E_\gamma \gtrsim 10^{13}$ eV.

At these high energies, the particle flux is extremely low (see the previous section). However, the individual Cherenkov pulses of these high-energy γ-ray cascades are rather strong. Therefore, an extended array of several hundred detector stations which are separated on the order of 100 m from each other was found to satisfy the desired balance between signal coverage, detection probability and effective area [46, 16].

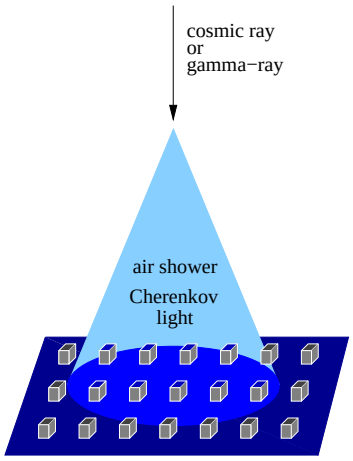

Figure 11: Schematic illustration of the working principle of the H$_i$SCORE detector. Image from [16].

Each H$_i$SCORE detector station will feature four large-diameter (20 cm) photomultiplier tubes pointed at the sky and surrounded by a *Winston cone*, a specially shaped metal reflector cone to optimize light collection and broaden the field of view. With the cones, the four PMTs make for a *light collection area* of 0.5 m^2 for each station [16]. At $E_\gamma \gtrsim 10^{13}$ eV, a H$_i$SCORE station will be triggered by a γ-ray's extensive air shower if it lies within 120 m of the shower core. Therefore, the station's *effective area* is about 40 000 m^2, or 0.04 km^2.

The H$_i$SCORE experiment aims for several 100 km^2 of effective area instrumented with one thousand to several thousand detector stations. In comparison with other past and planned gamma-ray observatories, it can hope to uncover new, extremely low-flux and high-energy γ-ray sources. Its high sensitivity and large energy range will give H$_i$SCORE a high potential for identifying Galactic PeVatrons and resolving their spectrum [17]. Also see Fig. 12 on the next page for a comparison with other experiments.

In order to minimize the material and organizational effort of the H$_i$SCORE array, self-sustaining stations, e.g. powered by solar energy and communicating wirelessly, would be preferable, but such a setup poses some difficulties. The large expanse of the array would require decentralized wireless mesh networking, which can be unreliable. Furthermore, the location of the array would need to have enough sunlight exposure, wind, or some other accessible source of energy to power the station [16].

Possible locations under consideration for the H$_i$SCORE experiment include: Tunka

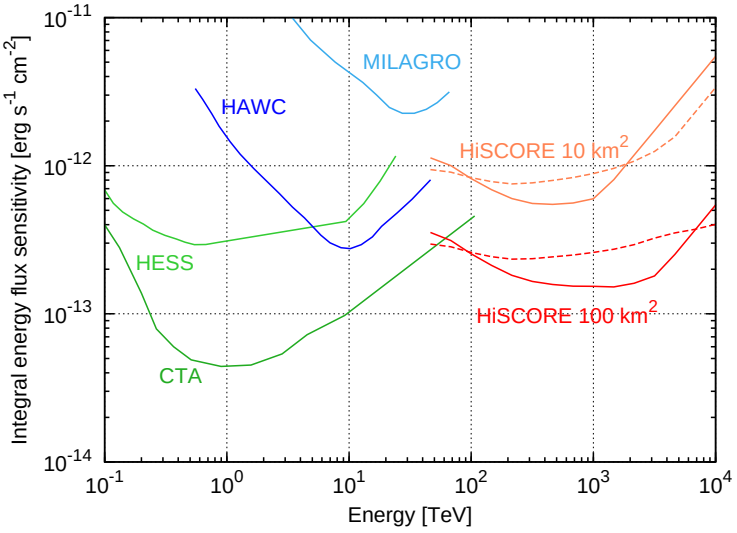

Figure 12: A comparison of the sensitivities of several gamma-ray observatories, including water, imaging and non-imaging Cherenkov detectors. The lines mark the minimum flux (integrated over all primary particle energies) detectable by the respective experiments. For the non-directed water Cherenkov detectors MILAGRO and HAWC as well as for H$_i$SCORE, a 5 year survey of some region of the sky is assumed, whereas the directed, imaging Cherenkov telescopes HESS and CTA were simulated to have observed every source in that region for 50 hours each. The dashed lines give H$_i$SCORE's sensitivity assuming that no gamma/hadron separation is undertaken. Image from [16].

Valley in the Russian Buryat Republic in south-eastern Siberia (the site of the TUNKA non-imaging Cherenkov detector array), the Pampa Amarilla site in western Argentina (the site of the Pierre Auger Observatory cosmic ray detector) and Fowler's Gap in New South Wales in south-eastern Australia (currently a wildlife research station) [16, 24].

The development and deployment of H$_i$SCORE is planned in several stages [45]:

Prototype Array The deployment of the first stations at the site of the TUNKA Cherenkov detector array in Russia is completed and their mechanical construction and electronic components are being evaluated. The setup still relies heavily on the infrastructure of the TUNKA array for reliability and long-term testing of the H$_i$SCORE station prototypes.

Engineering Array At this stage, 25 fully operational stations will be deployed at the TUNKA site, operating on their own data acquisition infrastructure under production use conditions. The Engineering Array will allow testing of all aspects of H$_i$SCORE in preparation for the final deployment.

Final deployment The final deployment of a large number of H$_i$SCORE detector sta-

tions will be realized in a specially selected and surveyed location with the proper support infrastructure and a station design adapted to meteorological and observational conditions at that location.

At the time of this writing, simulations of H$_i$SCORE's performance are promising [16] and construction of the Prototype Array is well underway: see the photograph of the very first station prototype's setup in Fig. 15 on page 25. One of the first signals recorded with this prototype station are shown in Fig. 16 on page 25. Several stations are now operational at the TUNKA site, and the Engineering Array will be erected at that same site until 2014. Despite some practical difficulties that come naturally with any such complex undertaking, H$_i$SCORE is set to deliver significant results to further our understanding of the universe.

In this work. The proposed signal processing and control flow layout of a H$_i$SCORE station is outlined in Fig. 13. The DRS4 Evaluation Board Version 3 is the readout hardware chosen for use with the Prototype Array. It is a multi-channel data acquisition device with high sampling frequencies of 1 to 5 GHz. Section 3 has a comprehensive introduction of the device.

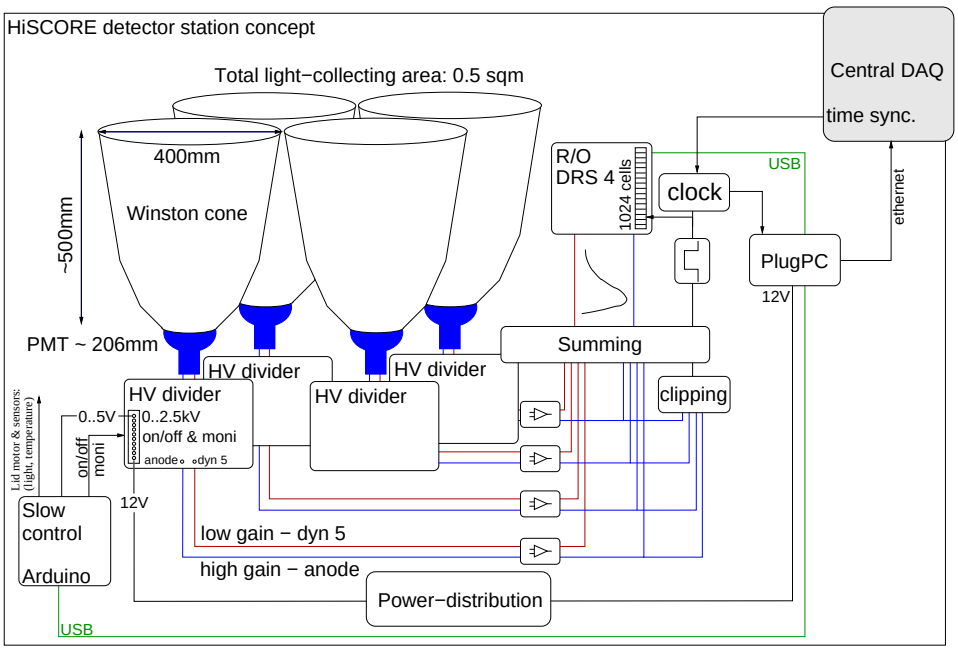

Figure 13: Schematic overview of the signal processing and control flow layout for a H$_i$SCORE station. This work is mainly concerned with the DRS4 readout and the time synchronization pictured clock at the top right of the image. Image from [46].

As explained in the previous section, precise timing is essential for H$_i$SCORE to function as a γ-ray observatory. As seen in Fig. 10, an EAS' Cherenkov signal must be resolved to at least 1 ns in order to detect the differences in the signals' rise time that enable gamma/hadron separation. The DRS4 Evaluation Board's high sampling rates can ensure this precision. Section 4 describes an investigation of its timing precision, with a focus on possible cross-channel delays. Furthermore, readout software is evaluated for its maximum possible readout frequency in section 5.

Another important timing-sensitive aspect of H$_i$SCORE is the the angular resolution of the detector, which depends on the quality of the time synchronization between the stations. Figure 14 shows the results of simulations of this dependency, giving the angular resolution of the detector in for different values of time jitter (the timing uncertainty of the system, explained further in section 3.3 on page 32). Section III describes a proposal for an analog time-tagging system that is designed to function with the DRS4 Evaluation Board in conjunction with a reference time (provided by a GPS receiver in the example presented, but ideally coming from a more precise source). An emulation of this system was tested and the results are presented.

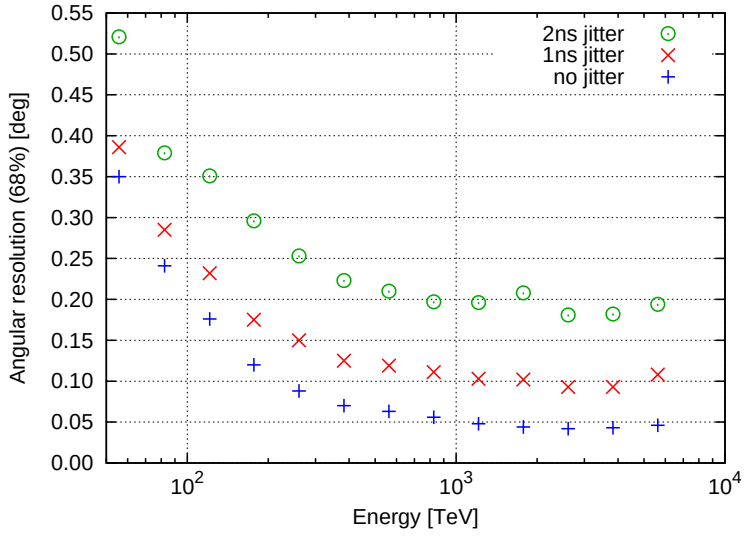

Figure 14: Simulation results for the angular resolution (to 1σ, meaning 68 % of events are correct to within the respective value) of the H$_i$SCORE detector for different time jitter values. Image and simulation from [16].

Figure 15: Photograph of the installation of the first H$_i$SCORE station at Tunka Valley, marking the beginning of H$_i$SCORE Prototype Array operations. Image from [24].

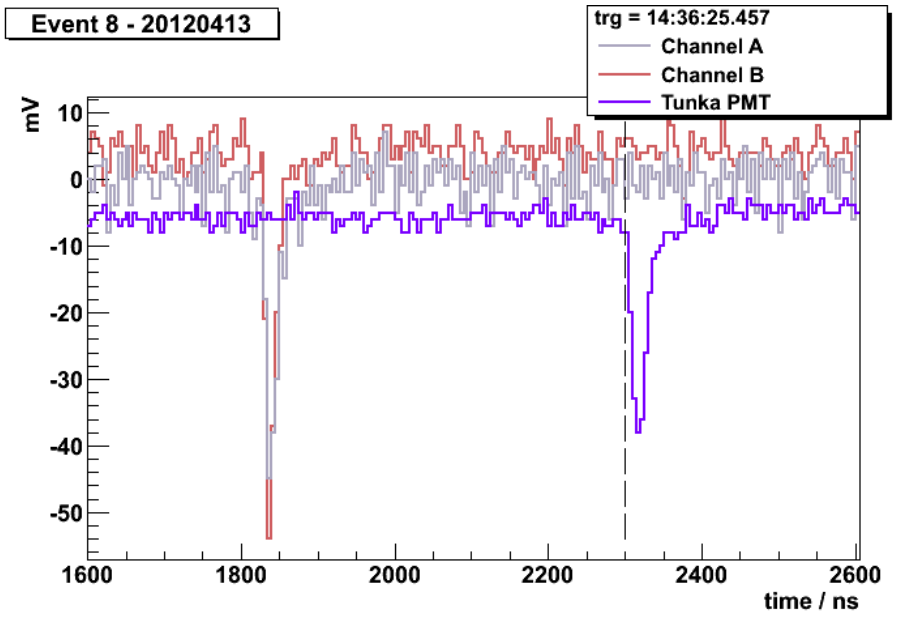

Figure 16: First light for the H$_i$SCORE detector: Pulses detected by the Prototype Array using the TUNKA array's trigger system, with TUNKA's recorded signal shown for comparison. Image from [24].

Part II.
H_iSCORE readout with the DRS4 chip

Now these points of data
make a beautiful line.

—GLaDOS

---

from *Portal*,
Valve Corporation (2007)

3. DRS4 hardware and operation

The DRS4 chip developed at Paul Scherrer Institut in Villigen, Switzerland (PSI) was chosen as the main readout hardware for the H$_i$SCORE experiment for its high sampling speed, multi-channel capability, and its compact form and inexpensiveness.

The developers of the DRS4 chip offer an Evaluation Board (EB)[†] for testing. For deployment in the the H$_i$SCORE Prototype Array, several Evaluation Boards were acquired and have been tested in this work. For later deployment of the Engineering Array, a custom-designed DRS4 readout board is under development.

This section describes testing of the DRS4 EB with regards to its timing precision and readout speed. From these investigations, insight is gained also on requirements for successful custom DRS4 readout hardware for H$_i$SCORE.

3.1. Basic principles

In the words of its developer [41, p. 1],

> The Domino Ring Sampler (DRS) is a switched capacitor array (SCA) capable of sampling 9 differential input channels at a sampling speed of 700 MSPS to 5 GSPS [...]. The analog waveform is stored in 1024 sampling cells per channel, and can be read out after sampling via a shift register clocked at 33 MHz for external digitization.

DRS stands for *Domino Ring Sampler*, indicating the basic operational principle of the chip. Every channel comprises 1024 readout cells, each with a small storage capacitor (0.15 pF). In data acquisition mode, the input signal is applied to the cell capacitors one after the other, effectively taking a sample reading of the input voltage at each moment a cell capacitor is connected by storing a corresponding charge in the capacitor (see Fig. 17 on the next page). Upon reaching cell 1023, readout goes on with cell 0, providing for continuous, circular readout with the last 1024 readout values always stored in the cell capacitors. The sampling frequency f_s with which the switch from one cell to the next occurs is variable from 0.7 to 5 GHz, corresponding to sampling at 0.7 to 5 GSPS (*gigasamples per second*).

When a trigger is received, the DRS4 switches from readout mode to writeout mode, in which the charge of the cell capacitors is measured and output as an analog voltage (see Fig. 18 on the following page).

For digitization, this analog output can then be routed through an analog-to-digital converter (ADC). The readout frequency for this operation can be set at the DRS4's shift register clock (SRCLK) pin to at least 10 MHz and at most 40 MHz, with ideal performance at 33 MHz [41]. At that frequency, there is always a dead time of at least $1024 \cdot (33\,\mathrm{MHz})^{-1} \approx 31\,\mu\mathrm{s}$ during which the signal is output.

[†] "DRS4 Evaluation Board" may from here on be abbreviated as DRS4 EB or just EB. Unless otherwise stated, this will always refer to the Evaluation Board Version 3.

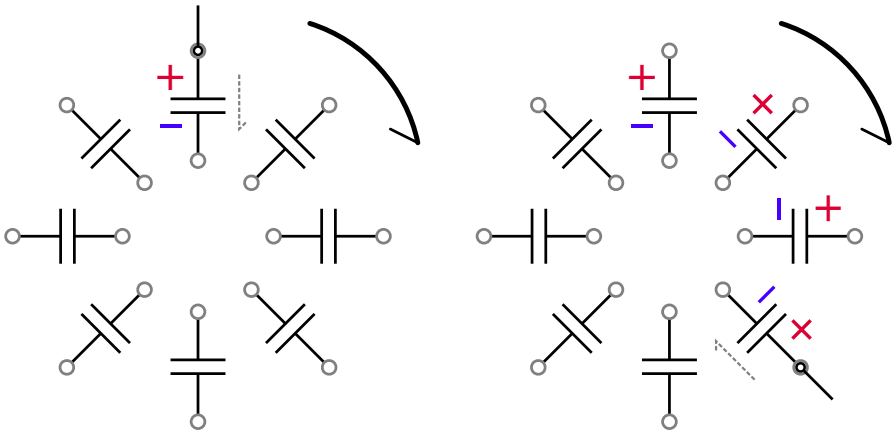

(a) $t = 0$ (b) $t = 4 \cdot (f_s)^{-1}$

Figure 17: Schematic illustration of the DRS4's working principle when reading a signal (writing to the cell capacitors). There are eight cells pictured where the DRS4 has 1024 cells for each channel, running in parallel.

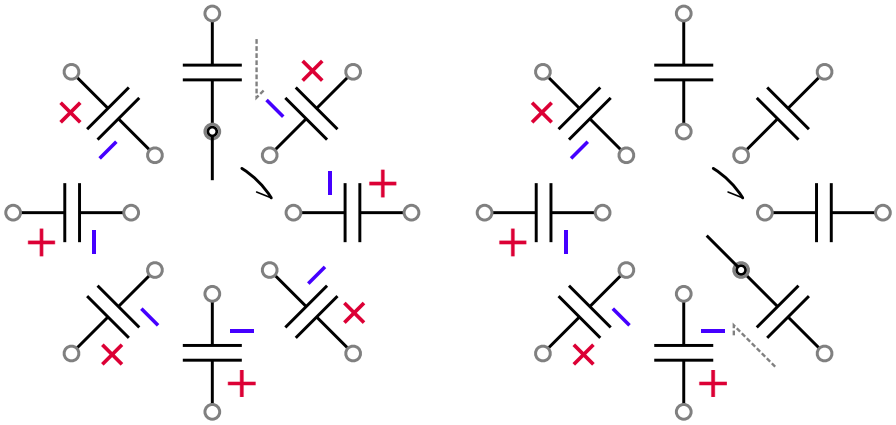

(a) $t = 0$ (b) $t = 4 \cdot (33\,\mathrm{MHz})^{-1}$

Figure 18: Schematic illustration of the DRS4's working principle when writing out the buffer (reading out the cell capacitors). There are eight cells pictured where the DRS4 has 1024 cells for each channel. On the DRS4 EB, the channels are read out in sequence, with one cell value digitized at a time by the central ADC.

As there are several channels to be read out, the DRS4 allows for two different digitization configurations: either all channels' values are output simultaneously, or the data is *multiplexed* by outputting the values of all channels sequentially through a single output. This presents a hardware/dead time tradeoff, where dead time is minimized when there are as many ADCs present as there are channels to be read out, or the dead time being larger by a factor equal to the number of channels when there is only one ADC.

In general, switched capacitor arrays (SCA) have the advantage of being considerably cheaper and less power-consuming than ADCs at comparable sampling speeds, with no need to sacrifice the number of channels for sampling speed. The DRS4 chip has a power consumption of about 90 mW per channel in a 4-channel chip at 5 GSPS [41], at a cost of $15 per unit for 10 000 units (2008 price for 8-channel units) [27].

The most high-speed ADC currently available from Texas Instruments is the 8-bit LM97600 with a power consumption of 3000 mW at 5 GSPS at a cost of $250 per unit for 1 000 units (December 2012 price). It is limited to one channel at 5 GSPS sampling speed, or 2 channels at 2.5 GSPS each, or 4 channels at 1.25 GSPS each. Competing products have equally high power consumption and cost, and are limited by the same sampling speed/channel number tradeoff.

The dynamic range of the DRS4's input is 1 V, natively ranging from 1.05 to 2.05 V. It can be shifted downwards by applying a *readout offset voltage (ROFS)* to the DRS4's ROFS pin of at most 1.6 V. Thus, the dynamic range can be set between the ranges of -0.55 to 0.45 V and 1.05 to 2.05 V [41, p. 9].

The noise of the cell readout is given as 0.35 mV after calibration [41, p. 3], corresponding to an effective precision of 11.5 bits over the dynamic range of the readout: $1\,\mathrm{V}/2^{11.5} = 0.345\,\mathrm{mV}$. Therefore, an ADC with at least 14 bits of precision ($1\,\mathrm{V}/2^{14} = 0.061\,\mathrm{mV}$) should be used for digitizing the DRS4's output, so as not to lose precision to digitizing granularity.

3.2. Evaluation Board

The DRS4 Evaluation Board provides power, run control, calibration circuitry, communications and convenient connectors for an included DRS4 chip, making for a compact, ready-to-use data acquisition (DAQ) unit with four input channels and a trigger input. Figure 19 on the next page shows an EB without its case.

Of the 9 channels on the DRS4 chip, one is connected to time calibration circuitry provided on the Evaluation Board. This setup makes use of the fact that time calibration needs to be performed only on one channel, but that this channel needs to be connected to a calibration signal (see the following subsection for details on time calibration). Four of the DRS4 channels are connected to the four input connectors. The remaining four channels of the chip are not connected.[†] The external trigger input

[†]The remaining four channels can be hardwired to the four input channels, providing an effective channel depth of 2048 cells each, but this is not implemented by default in H$_i$SCORE's EBs.

of the DRS4 chip is connected to a trigger buffer circuit that feeds into the run control FPGA[†].

As seen in Fig. 20 on the following page, spikes sometimes occur in the signal. This is a known effect of the EB up to version 3. It reduces the usefulness of internal triggering, because a spike can be interpreted as a rising or falling flank and lead to bogus triggering.

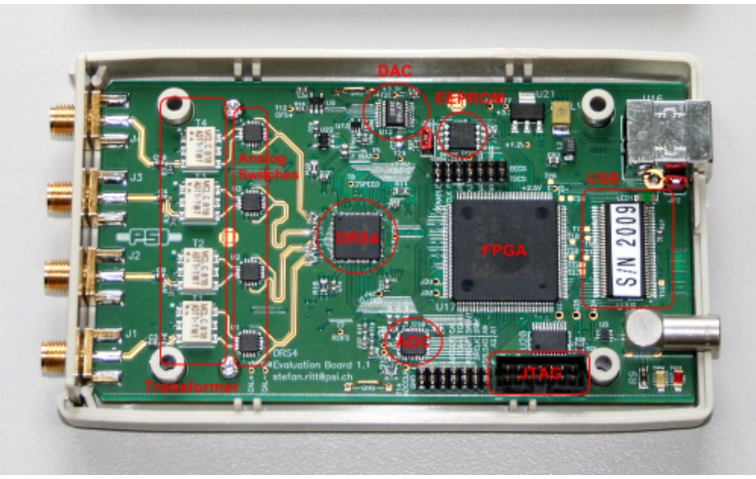

Figure 19: A photograph of the interior of an early version of the DRS4 Evaluation Board. The I/O connectors shown are identical to those of the version 3 board used in this work. Note the DRS4 chip situated at the center of the board. The four SMA jacks to the left are the input channel connectors. The LEMO 00 jack at the bottom right is the external trigger input connector. The USB-B jack at the top right is used for the data connection as well as supplying power. Image from [39].

The run control FPGA loads its instructions from a permanent memory module (EEPROM) that can be reprogrammed through a computer using a JTAG connection[‡]. The *firmware upgrades* discussed later in this work are upgrades of those instructions stored on the EEPROM.

The DRS4 Evaluation Board uses a 14-bit ADC (an Analog Devices model AD9245 [1]) with a granularity of $1\,\mathrm{V}/2^{14} = 0.061\,\mathrm{mV}$. This minimum granularity is also called the Least Significant Bit (LSB) value. The ADC's Differential Non-Linearity[†] is given

[†]Field-Programmable Gate Arrays (FPGAs) are integrated circuits whose function can be customized by programming. They usually feature many input and output connectors, making them highly versatile and flexible.

[‡]JTAG stands for Joint Test Action Group, and has become a popular name for technology developed by this group. This technology is the Standard Test Access Port and Boundary-Scan Architecture, originally a test protocol for printed circuit boards that is now widely used for communication with integrated circuits.

[†]Differential Non-Linearity (DNL): Deviation from an ideal fit of one-bit steps to a continuous signal that occurs *between consecutive steps*.

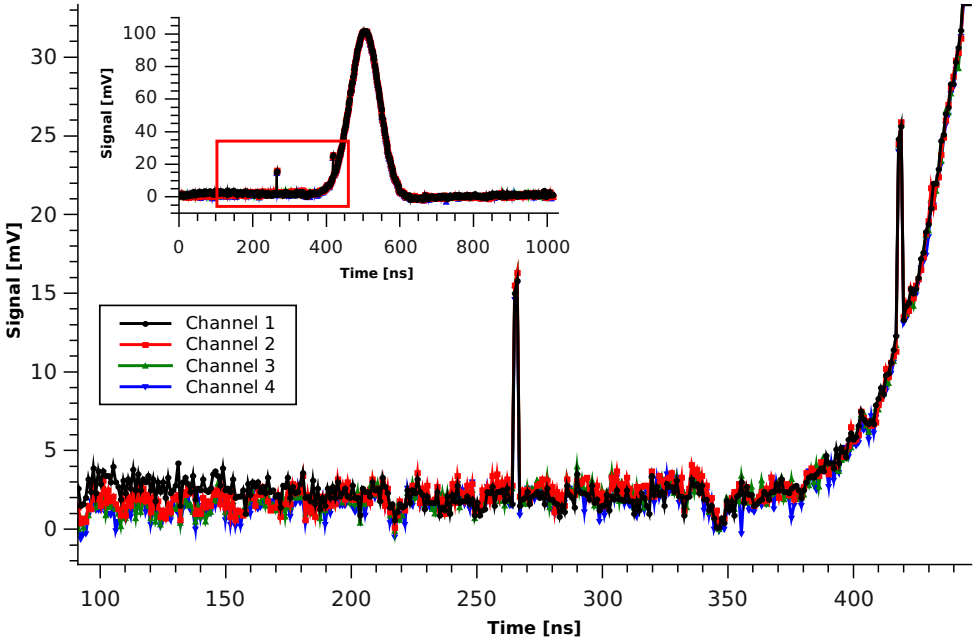

Figure 20: Intermittent kinks in a measured Gaussian curve. The effect is always additive and apparently of absolute value. It is known to be caused by the DRS4 Evaluation Board itself. Inset: An overview of the entire dataset. The red rectangle indicates the area detailed in the larger plot.

as typically $\pm 0.50\,\mathrm{LSB}$ and at most $\pm 1.00\,\mathrm{LSB}$, while its Integral Non-Linearity[‡] is given as typically $\pm 1.40\,\mathrm{LSB}$ and at most $\pm 5.55\,\mathrm{LSB}$ [1]. Accordingly, the worst case scenario is that the non-linearity of the DRS4 EB's sampling is of the same order of magnitude as the cell noise.

As there is only this one ADC present on the Evaluation Board, the readout of cell data from the DRS4 chip is performed in multiplexing mode, at the optimal 33 MHz readout frequency. Therefore, the readout dead time dead is always at least

$$4 \cdot 1024 \cdot (33\,\mathrm{MHz})^{-1} \approx 124.1\,\mu\mathrm{s}.$$

A 16-bit DAC is also present, serving multiple purposes. For one, it connects to the DRS4's ROFS pin through a low-noise buffer for input range shifting. Secondly, it generates the voltages used for voltage calibration.

The USB connector serves as both data connection and power supply, with a nominal voltage of $5\,\mathrm{V} \pm 5\,\%$ and a maximum current of 500 mA [7, p. 181]. An on-board USB

[‡]Integral Non-Linearity (INL): Deviation from an ideal fit of one-bit steps to a continuous signal that occurs *over the entire digitization range.*

controller provides the data connection used to transfer data to a computer. Section 5.1 on page 43 gives further details on this data connection.

The DRS4 EB is shipped with a comprehensive software library that includes several different control programs and implementations of DAQ use cases as well as source codes and libraries that allow for the development of custom software. The following programs were used extensively for this work:

a) `drsosc`, a graphical application simulating the behavior of an oscilloscope using the EB's four input channels and trigger input.

b) `drscl`, a command-line interface for control and configuration of the EB's core functions and firmware.

c) `drs_exam`, a basic command-line tool for simple data acquisition. This was modified into the main software for several trial measurements with the DRS4 EB in [9] and in this work.

3.3. Timing uncertainties and calibration

Every electronic communications and data processing system is subject to *jitter*, which is a term used to describe various effects that negatively impact a system's timing accuracy. Jitter usually consists of two components: *systematic* and *thermal* (random). While systematic jitter can be caused by interference from other signals or components (like a power supply) or design errors or limitations, thermal jitter is a physical effect attributed to the thermal excitation of charge carriers. No system is ever completely jitter-free.

The two most significant systematic effects that introduce jitter in the DRS4 chip are *aperture jitter* and the *domino stop time* as explained below.

Aperture jitter. This effect introduces a timing uncertainty on the order of 100 ps per cell. It is composed of the *fixed pattern aperture jitter* and the *random aperture jitter*. While the former is caused by a mismatch of the transistors in different cells, and is thus fixed for every chip, the latter is variable and differs with each domino cycle [41, p. 9].

Figure 21 on the following page shows a schematic illustration of this effect. The cells do not have the expected width of $(f_s)^{-1}$. Instead, the n-th cell deviates from this expected value by some time $\mathrm{TD}_n = \Delta t_1 - (f_s)^{-1}$. The integral non-linearity of all n channels is then:

$$\mathrm{TI}_n = \left(\sum_{i=1}^{n} \mathrm{TD}_i \right) - n \cdot (f_s)^{-1}.$$

This integral nonlinearity is usually on the order of 1 ns, but is higher for lower values of f_s.

Note that correcting for the integral nonlinearity alone is insufficient: The different TD_i might cancel out while the signal is still distorted. The solution proposed by the developer in [40] is to sample a high-precision signal to calibrate out the fixed pattern aperture jitter and to furthermore minimize the random aperture jitter statistically. The DRS4 Evaluation Board features a 240 MHz clock that is sampled to measure the *effective bin width* $(f_s)^{-1} + \mathrm{TD}_i$ for each cell, which are then corrected for.

Domino stop time. This refers to a delay between a trigger and the beginning of the readout process. A random delay on the order of 2 to 3 ns occurs because the switch from cyclical (also called *domino*) cell writing to reading is not instantaneous. Additionally, the switch from write mode to read mode can only occur upon a switch from one cell to another, resulting in a native timing uncertainty of $(f_s)^{-1}$.

The developer suggests making timing relative to the internal reference clock of the chip instead of the trigger [41, p. 9]. This can be achieved by programming an accompanying FPGA to keep track of the clock and the signal. A simpler solution is to sample the trigger signal in one of the input channels, along with the data (for an example, see Figure 36 on page 60). That way, the relative position can be reconstructed from the trigger signal itself, fitting it if necessary. The DRS4 Evaluation Board software `drsosc` offers such a feature for events triggered on a sampled channel (but not, obviously, for external triggering, where the trigger channel is not sampled).

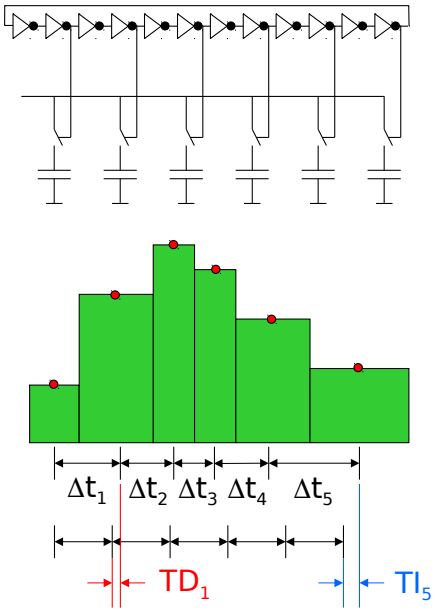

Figure 21: Schematic illustration of the DRS4's *aperture jitter* and related values. Image from [40].

4. Cross-channel signal delay

Short summary: Measurements were made to find any difference in signal arrival time between the channels of the DRS4 Evaluation Board. Normally distributed run time differences were found and in part attributed to differences in cable length of $\lesssim 1\,\mathrm{cm}$. After correction, the remaining run time differences on the order of 10 to 100 ps show reasonable consistency in magnitude and spread, both for different readout frequencies and over time.

4.1. Setup: Measurement and calculation

For measuring channel run time delays, a signal source generating a Gaussian curve was chosen. In contrast to a continuous signal like a sine wave, isolated Gaussian peaks are less likely to be distorted by signal reflections. Also, tests showed that isolated Gaussian peaks from a function generator could be fitted more accurately than sine signals. The method used will be called the *Gauss fitting* method hereinafter.

The experimental setup, as seen in the schematic in Figure 23 and the photograph in Figure 24 on the following page is as follows: Gaussian peaks of about 200 ns in width (100 ns at full width, half maximum) are produced by the function generator at a frequency of 1.25 MHz ($= 800\,\mathrm{ns}^{-1}$) and distributed to the four input channels of the EB using simple cable couplings. A square signal in phase lock with the Gaussian signal triggers the EB on its external trigger input to avoid internal triggering, which is susceptible to signal noise disturbance (see Fig. 20 on page 31).

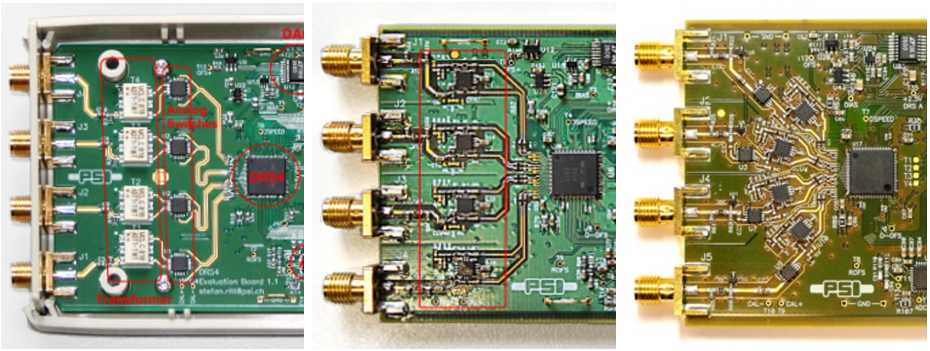

(a) DRS4 EB v1 (b) DRS4 EB v3 (c) DRS4 EB v4

Figure 22: Photographs of the input circuitry of three different revisions of the DRS4 EB. Note how the wires between the input connector and the DRS4 chip differ in length for different channels, constituting a source for cross-channel signal delay. Observe also how the layout was revised in later revisions to minimize this effect. Images from [39].

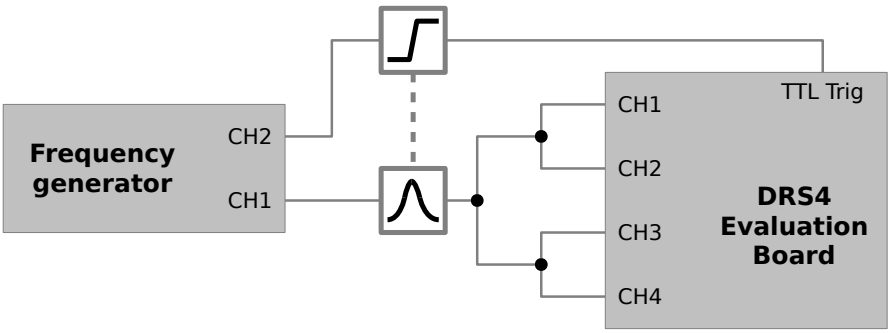

Figure 23: Schematic of the experimental setup for cross-channel time jitter measurements by the *Gauss fitting* method. The dashed line indicates phase lock between the two output channels.

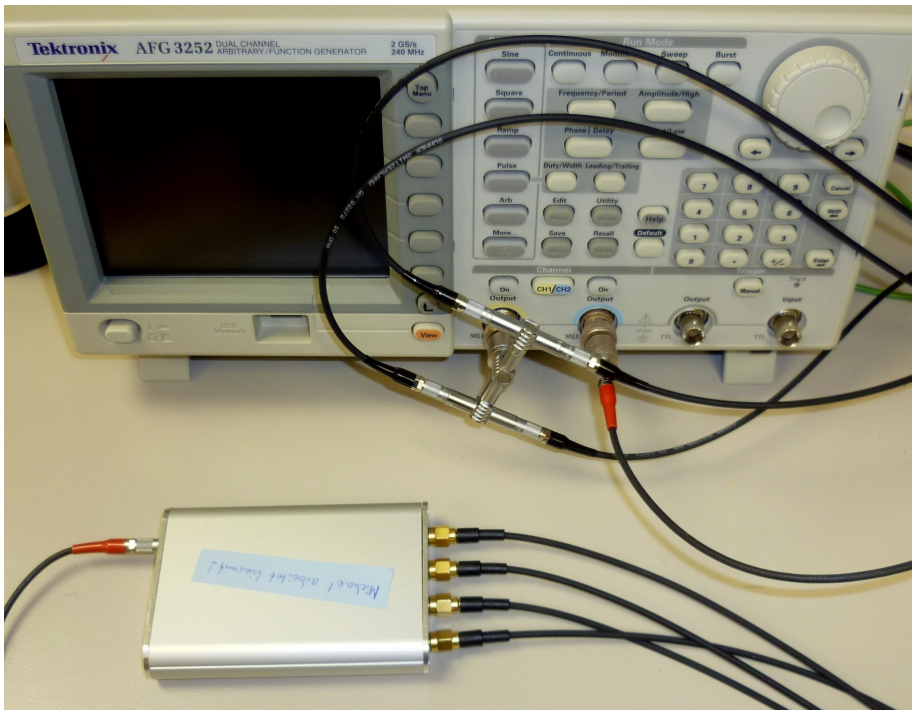

Figure 24: Photograph of the experimental setup for cross-channel time jitter measurements by the *Gauss fitting* method. Note the cable couplings in the center of the image.

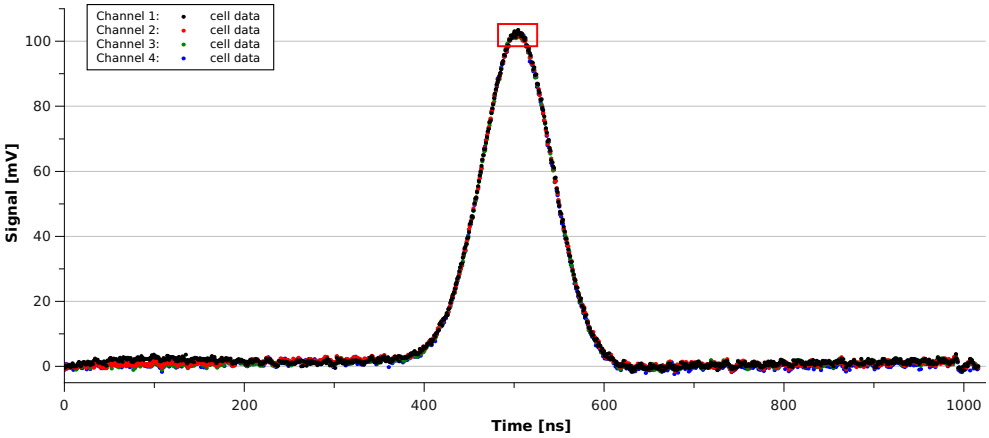

(a) Overview of the entire dataset, cell data only.

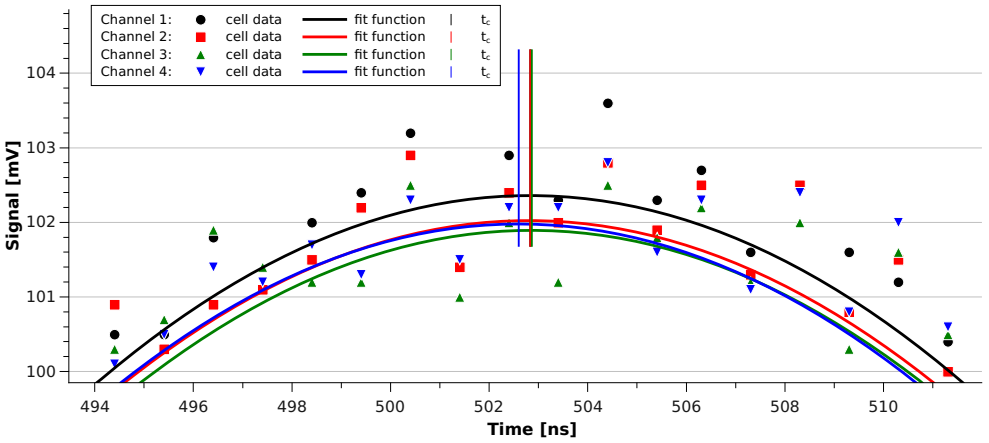

(b) Detailed view of the area outlined by the red rectangle above, along with fit functions and the position of the t_c fit parameters. Fit errors of the t_c parameters are not visible at this scale.

Figure 25: An event recorded for analysis with the Gauss fitting method at $f_s = 1\,\mathrm{GHz}$. The event was chosen for exhibiting a relatively large peak position difference: $\Delta_{34} \approx 260\,\mathrm{ps}$ (with $\sigma_{\Delta_{34}} = \sqrt{\sigma_{c,3}^2 + \sigma_{c,4}^2} \approx 88\,\mathrm{ps}$). In both plots, the cell data error of $\pm 1\,\mathrm{mV}$ is omitted for visibility.

Each channel is separately fitted with a Gaussian function, of whose fit parameters only the *peak position* t_c is of further interest:

$$f(t) = Y_0 + A \cdot \exp\left(-\frac{(t - t_c)^2}{2 \cdot W^2}\right).$$

For each pair of channels m and n, the *fit peak position difference* Δ_{mn} is calculated.[†] It is a measure for how much the signal in channel n is delayed with respect to channel m:

$$\Delta_{mn} = t_{c,m} - t_{c,n}.$$

With σ_c^2 being the variance of the peak position t_c's fit error as given by the fit routine, the variance for Δ_{mn} is

$$\sigma^2_{\Delta_{mn}} = \sigma^2_{c,m} + \sigma^2_{c,n}.$$

Measurements were made in *series* of about 1 000 consecutive events.[‡] For each pair of channels, all Δ_{mn} of a series were plotted in a histogram as seen in Fig. 26. As expected, the Δ_{mn} are normally distributed, and were fitted with a normal distribution

$$f(\Delta_{mn}) = Y_0 + A \cdot \exp\left(-\frac{(\Delta_{mn} - d_{mn})^2}{2 \cdot \Sigma^2_{mn}}\right).$$

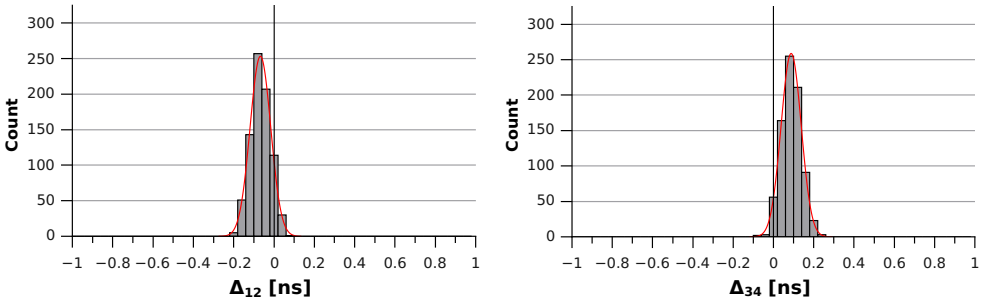

Figure 26: An example of two peak position difference histograms (Δ_{12} and Δ_{34}) of a series with 808 events, along with their normal distribution fits. The fit parameters are $d_{12} = -67.5\,\text{ps}$ with $\Sigma_{12} = 51.2\,\text{ps}$ and $d_{34} = 88.0\,\text{ps}$ with $\Sigma_{34} = 50.0\,\text{ps}$.

[†] There are $\binom{2}{4} = 6$ pairs of channels: Δ_{12}, Δ_{13}, Δ_{14}, Δ_{23}, Δ_{24} and Δ_{34}.

[‡] "Consecutive" in the sense of the actual readout, where several hundred events are recorded in several seconds, *not* in the sense of the signal source, where several hundred events are generated in less than 1 ms.

Two fit parameters for these distributions are of interest: The *central signal run time difference* d_{mn} and the *signal run time difference spread* Σ_{mn}. Their fit errors are generally $\lesssim 1.5\,\mathrm{ps}$ and will not be regarded further.

Σ_{mn} depends on two components: Statistical errors of the Δ_{mn}, and a physical (systematic) error of the Evaluation Board $\Sigma_{\mathrm{EB},mn}$, which is the actual quantity of interest. The statistical component for a series of N events, depends on N many values of $\Sigma_{\Delta_{mn}}$, which in turn depend on $2N$ many values of $\sigma_{t_{c,i}}$:

$$\begin{aligned}\Sigma_{mn} &= \Sigma_{mn}(\sigma_{\Delta_{12},1},\ldots,\sigma_{\Delta_{34},N},\Sigma_{\mathrm{EB},mn})\\ &= \Sigma_{mn}(\sigma_{t_{c,1},1},\sigma_{t_{c,2},1},\ldots,\sigma_{t_{c,3},N},\sigma_{t_{c,4},N},\Sigma_{\mathrm{EB},mn})\end{aligned}$$

This relationship was not resolved exactly, and so $\Sigma_{\mathrm{EB},mn}$ cannot be extrapolated from the fitted Σ_{mn}. Still, it is certain that:

$$\Sigma_{mn} > \Sigma_{\mathrm{EB},mn}$$

This way, at least an upper bound for the hardware-related spread is known.

4.2. Cable mismatch correction

It was found that the custom-manufactured cables used to connect the function generator to the DRS4 EB were not all of the same length: one was visibly shorter than the others. This was recognized as a possible cause for inconsistencies hitherto observed in the results. The mentioned cable was marked “shorty” and its effect corrected for as shown in Fig. 27 on the next page.

When measuring the signal run time delay before and after exchanging two cables of different lengths, the offset between the two measurements corresponds to twice the cable delay:

$$t_{cB} - t_{cA} = 2d_{\mathrm{cable}}.$$

The cable delay can then be corrected for by taking the arithmetic mean of the two measurements

$$t_{cA} + d_{\mathrm{cable}} = t_{c,\mathrm{true}} = t_{cB} - d_{\mathrm{cable}}.$$

For a consistent overview of the effects described above, measurements were made for different:

a) channel pairs: d_{12}, d_{13}, d_{14}, d_{23}, d_{24}, d_{34}

b) readout frequencies: $f_s = 1\,\mathrm{GHz}$, $f_s = 5\,\mathrm{GHz}$

c) pairs of cables: „shorty“ and average-length, average-length and average-length

The combined results for d_{cable} (see Table 1 on the following page) correspond remarkably well to the widespread rule of thumb that analog signals propagate through

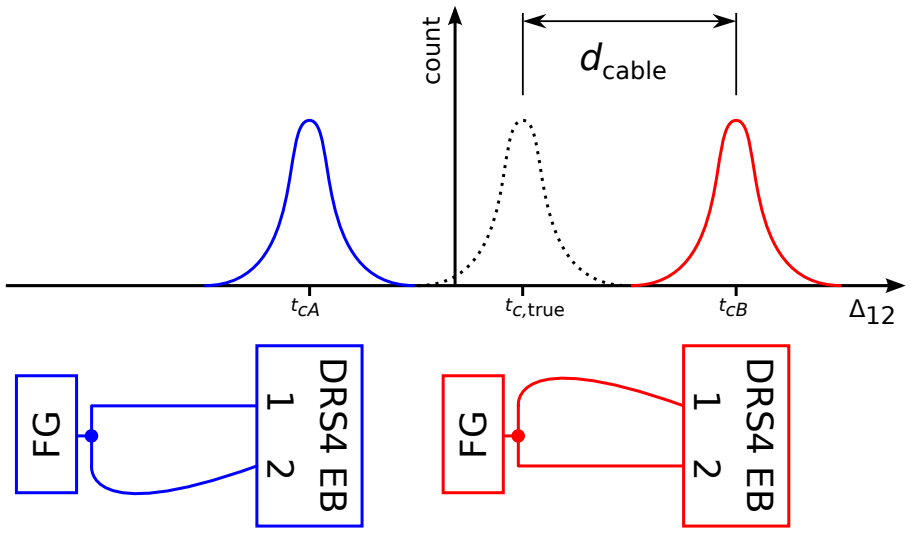

Figure 27: Simplified schematic of the method used to correct for cable length differences. The blue diagram and curve (setup A) corresponds to the run with the shorter cable on channel 1, red (setup B) to the shorter cable on channel 2.

coaxial cables at a speed of $\frac{2}{3}c$ [29]. From visual inspection, the cable dubbed "shorty" was found to differ in length by

$$\Delta s_{\text{cable}} = (10 \pm 1)\,\text{mm}$$

from the other cables. The results of the measurement described above, according to the $\frac{2}{3}c$ rule of thumb, give a cable length difference of

$$\Delta s_{\text{cable}} = (63.5 \pm 2.9)\,\text{ps} \cdot \frac{2}{3}c = (12.7 \pm 0.6)\,\text{mm}.$$

This very good agreement can be taken as a confirmation of the validity of the *Gauss fitting* method.

As far as visual inspection warrants, the average-length cables differ in length by no more than 1 mm. Yet, the Δs_{cable} for the tested pair of average-length cables is:

Table 1: Results of the cross-channel signal delay measurements: Cable delay. The errors are the population standard deviation of all values measured.

		1 GHz	5 GHz	combined
d_{cable}	shorty	(60.8 ± 0.9) ps	(66.1 ± 0.9) ps	(63.5 ± 2.9) ps
	normal	(11.9 ± 1.2) ps	(8.2 ± 0.6) ps	(10.0 ± 2.1) ps

$$\Delta s_{\text{cable}} = (10.0 \pm 2.1)\,\text{ps} \cdot \frac{2}{3}c = (2.0 \pm 0.4)\,\text{mm}.$$

Aside from concluding that visual inspection is inadequate, the results can also be interpreted such that there is an absolute offset of about 10 ps ($\widehat{=}$ 2 mm) to the delay, in which case both the visual and the statistical results can be reconciled. This hypothesis could, however, only be tested if precisely matched cables were available.

4.3. Results: Magnitude and stability

Signal run time differences between different channels of the DRS4 EB were always observed as following a normal distribution around some central value d_{mn} with a spread Σ_{mn}, both on the order of 1 to 100 ps. Table 2 gives an overview of those quantities after cable mismatch correction.

For all pairs of channels, the magnitude of the spread Σ_{mn} is rather large when compared to the offset $t_{c,\text{true}}$. For some pairs of channels, these values are even of the same order of magnitude. Since this normally distributed error cannot be corrected simply with an absolute offset, Σ_{mn} has to be considered jitter that adds to the overall timing uncertainty of any measurement made with the DRS4 EB.

Table 2: Channel run time differences and spread for two different readout frequencies. Measurements were made with two different sets of cables and their mismatch corrected for each time.

		1 GHz		5 GHz	
		$t_{c,\text{true}}$	spread	$t_{c,\text{true}}$	spread
d_{12}	shorty	117.9 ps	28.5 ps	114.4 ps	12.2 ps
	normal	119.4 ps	25.3 ps	112.5 ps	14.0 ps
d_{13}	shorty	170.0 ps	26.2 ps	161.5 ps	12.3 ps
	normal	169.1 ps	37.4 ps	161.7 ps	14.2 ps
d_{14}	shorty	198.1 ps	28.3 ps	170.2 ps	13.7 ps
	normal	196.8 ps	31.5 ps	168.7 ps	16.1 ps
d_{23}	shorty	47.1 ps	29.2 ps	44.7 ps	11.8 ps
	normal	46.8 ps	45.8 ps	46.3 ps	13.3 ps
d_{24}	shorty	75.5 ps	30.3 ps	54.7 ps	11.3 ps
	normal	76.8 ps	31.7 ps	54.4 ps	13.7 ps
d_{34}	shorty	22.4 ps	25.4 ps	7.2 ps	10.7 ps
	normal	24.9 ps	26.9 ps	4.7 ps	11.6 ps

The spread is systematically smaller for measurements made with $f_s = 5$ GHz as opposed to 1 GHz, which can be expected given the nature of the timing uncertainties

(see section 3.3 on page 32). It is also noteworthy that all d_{1m} are larger than those between channels other than 1, by at least $d_{12} - d_{23} \approx 50\,\text{ps}$ and at most $d_{14} - d_{34} \approx 170\,\text{ps}$. These effects are probably due to the design of the chip or the Evaluation Board (cf. Fig. 22 on page 34).

Figure 28 on the following page shows changes observed in d_{mn} and Σ_{mn} over several hours. Between consecutive measurement series, the setup was not altered or powered off. Two such long-time sequences were recorded on different days.

The d_{mn} as observed over time appear to show some random jitter of about 3 ps in magnitude, but little or no absolute drift.

The Σ_{mn}, on the other hand, clearly exhibit an absolute drift with time as well as jitter. After a rise from 35–40 ps to 50–55 ps, the slope decreases and the values steadily rise to 60–65 ps within a few hours. As is visible in the Σ_{mn} day 1 curves as opposed to day 0, the slope is greater in both parts of the curve when readout is performed more frequently.

These observations are consistent with thermal jitter effects of the DRS4 chip or the Evaluation Board. With time and repeated readout operations, the temperature rises and the Σ_{mn} get larger as thermal jitter increases. It is not obvious without careful study of the EB's components and layout which parts exactly effect this apparently thermal phenomenon.

Furthermore, coaxial cables are known to suffer from temperature-dependent phase drifts (i.e. changes in signal run time). Many cables contain Teflon™ as insulation material, which undergoes a molecular phase transition at room temperature, affecting its dielectric constant ϵ_r. Between 18 and 22℃, delay shifts of up to 1 picosecond per ℃ and meter of cable can occur [8]. Some systematic drift of the d_{mn} might be due to this effect. On the other hand, cables of less than 2 m in length were used and the laboratory was not exposed to sunlight, so the contribution is not likely to be larger than 5 ps and is not visible in Figure 28.

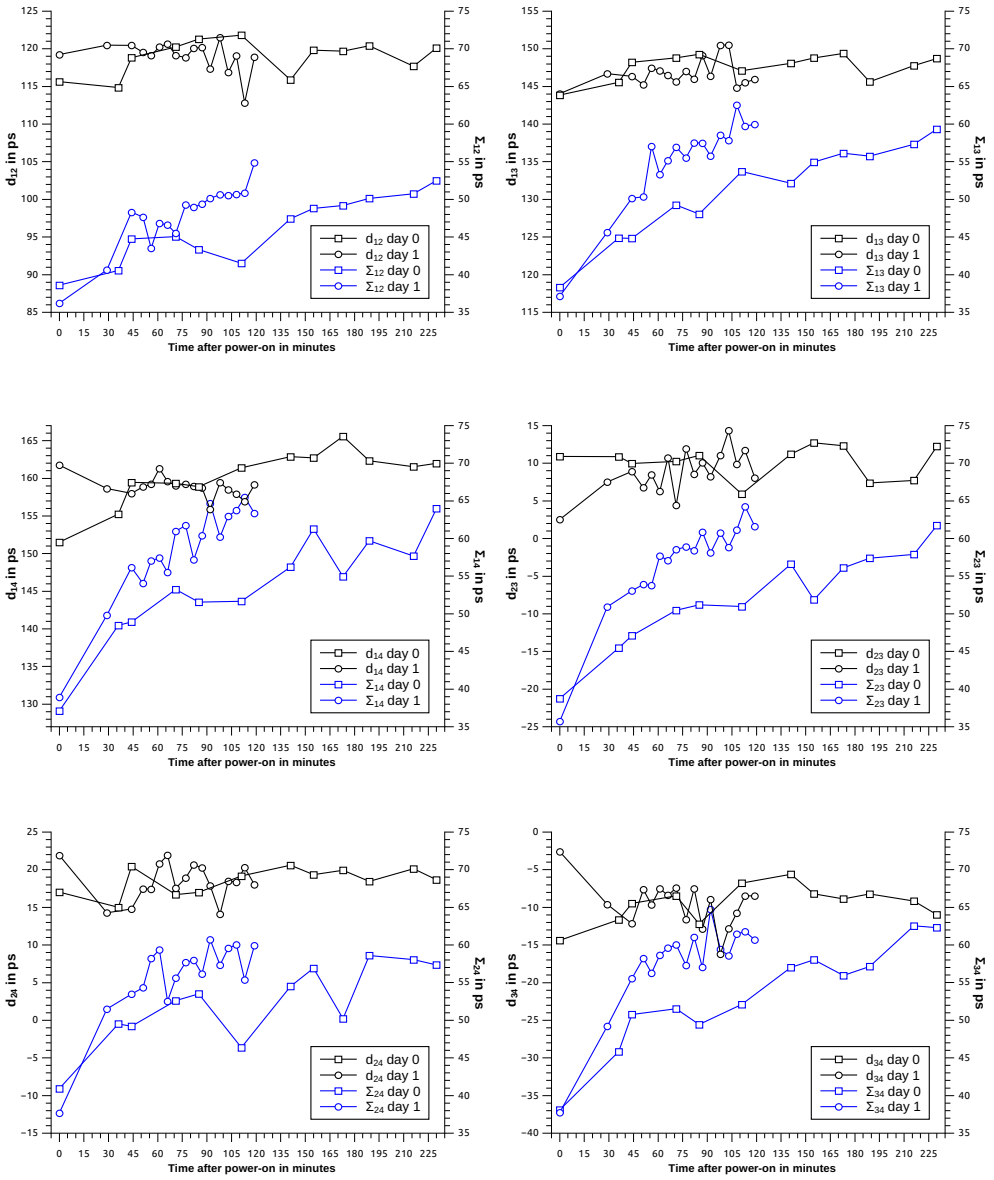

Figure 28: Plots of data from two sets of measurements, each a sequence of measurement series of 1 000 events, set several minutes apart and gathered over several hours. Note that the scales of all vertical axes are identical, except for absolute offsets. Each plot shows data for one pair of channels. d_{mn} and Σ_{mn} fit errors lie within the expanse of the data point symbols. Note that no cable mismatch correction was applied for this investigation of relative changes with time.

5. Data readout

Short summary: An effort was made to improve upon the findings in [9] with respect to the readout frequency of the DRS4 Evaluation Board. Using a more powerful computer and implementing several optimizations of the readout code, a readout frequency of 525 Hz was achieved, which is very close to the Evaluation Board's native limit.

5.1. Readout frequency

If a trigger causes data to be recorded for a sampling time t_s, after which a dead time t_{dead} elapses before the next trigger can be processed, the *maximum readout frequency* $f_{\max}$ and the actual, momentary *trigger frequency* f_t are related thusly:

$$f_t \leq f_{\max} = \frac{1}{t_s + t_{\text{dead}}}.$$

In an ideal system with no dead time, the maximum readout frequency would be the inverse of the sampling time:

$$f_{\max,\text{ideal}} = \frac{1}{t_s}.$$

For continuous triggering, i. e. $f_t = f_{\max}$, there would be continuous sampling. Such a mode of operation is very useful in examining the signal background and collecting minimum bias data. However, the enormous volume of data collected entails practical problems.

In any case, continuous readout cannot be realized with the DRS4 EB, both because of the basic operational principle of the DRS4 chip (see section 3 on page 27) and because of the EB's mode of communication. The EB uses a USB connection, and its firmware operates in such a way that only a single event is transferred, and only upon a request from the computer.

For USB connections, the basic unit of data transfer is the *frame*, which is defined to be 1 ms ± 500 ns long [7, p. 126]. As a result, there can be no less than a 2 ms delay between receiving an event and receiving the next one, since the computer has to wait for the request to be sent and the event data to be received in two separate frames of 1 ms duration each.

This limits the readout frequency to about 500 Hz, which corresponds to a far smaller data volume than the USB connection's theoretical transfer capacity of 20 MB/s would allow. While modern High Speed (USB 2.0) and Super Speed (USB 3.0) protocols divide the frame into 8 subframes of only 125 μs duration each, the EB does not make use of this functionality.

In practice, the DRS4 EB's readout frequency can also be dominated by the performance of the computer and the code used to control the readout, and thus be even lower than 500 Hz. Previous tests for H$_i$SCORE, as described in [9], used a GuruPlug

Table 3: Maximum achievable readout frequency (approximate, with writeout to disk) for different computers and different readout software. Readings marked with † were taken with upgraded firmware as described in **Optimization: Upgrading the EB's firmware** on this page.

	GuruPlug	Office PC
`drs_exam` as distributed with the EB	29 Hz	200 Hz
`drs_exam_modif_cast_bin_2` as in [9]	79 Hz	–
`drs_speedtest` as in this work	89 Hz†	525 Hz†

Server Plus mini-computer† and found upper limits for the readout frequency much lower than tests performed for this work on a modern office computer‡.

5.2. The `drs_speedtest` software

For this work, the same approach as in [9] was taken: The `drs_exam` software as distributed with the EB was modified to serve as a benchmark for the readout frequency and optimized for maximum performance through different measures. This section describes the steps taken to achieve the results presented here. The source code of the resulting program called `drs_speedtest` is given in Appendix B.1 on page 72.

Below, five optimization measures implemented in `drs_speedtest` are described. An overview of the performance gains achieved is given in Table 4 on the following page. It is important to note, however, that the magnitudes of these effects are interdependent: implementing them in a different order would have produced different $\Delta f_{\max}$ for each step, so the numbers cannot be considered absolute.

Optimization: Writing data in binary format. As discussed in [9], storing data in binary format instead of ASCII data not only minimizes the data volume, but also reduces the time spent writing the data to permanent memory. Furthermore, no conversion of numerical data to strings is necessary and the data can be copied directly from memory to storage.

Optimization: Upgrading the EB's firmware. H$_i$SCORE received its main shipment of the DRS4 Evaluation Board Version 3 in 2010. These boards came with firmware revision 15453 installed. Upgrading the firmware to revision 17147, which was released in 2011 as the final revision for the EB Version 3, raised the upper limit of the readout frequency significantly.

Optimization: Parallelizing writeout. In order to avoid waiting for event data to be written to permanent memory before another event can be read out, the writeout can

†Specifications: 1.2 GHz ARM processor by Marvell and 512 MB of DDR2 memory, 32-bit Linux.
‡Specifications: Dual-core 2.66 GHz processor by Intel and 8 GB of DDR2 memory, 64-bit Linux.

be handed over to a thread separate from the readout software. Such a procedure is useful as long as a single writeout operation takes more time a single readout operation. Threaded writing operations were implemented in `drs_speedtest` by using an adaptation of `asyncwriter` [37]. An increase in readout frequency was not seen on the system used for testing. Still, parallelized writeout will increase performance for environments with slower writeout (e.g. over a network connection).

Table 4: Improvements to the unmodified readout with `drs_exam` in chronological order and their impact on readout performance, using the Office PC as described on the previous page. **Note:** The magnitude of the effects depends on the order of implementation and is not absolute.

		$(\Delta) f_{\max}$
`drs_exam` without modification		200 Hz
Optimization: Writing data in binary format	(p. 44)	+180 Hz
Optimization: Upgrading the EB's firmware	(p. 44)	+110 Hz
Optimization: Avoiding `short int` casts	(p. 46)	+25 Hz
Optimization: Avoiding repeated time array readout	(p. 46)	+10 Hz
Optimization: Parallelizing writeout	(p. 44)	±0 Hz
`drs_speedtest`		525 Hz

`drs_speedtest` allows for the deactivation of all code pertaining to data writeout, in order to determine the overhead produced by writeout as opposed to reading and immediately discarding events. While the maximum achieved readout frequency with writeout is 525 Hz, the maximum readout frequency without writeout is about 535 Hz. The additional dead time introduced by writeout is thus

$$t_{\text{dead,wo}} \approx \frac{1}{525\,\text{Hz}} - \frac{1}{535\,\text{Hz}} \approx 36\,\mu\text{s}.$$

These values can be considered both an important improvement over the findings in [9] and a solid upper limit to the EB's readout capabilities. $f_{\max}$ is slightly above the limit imposed by the USB protocol and the $t_{\text{dead,wo}}$ is smaller by almost two orders of magnitude (see Table 5).

Table 5: Comparison of readout frequencies and writeout dead time between [9] and this work. It is important to recall the different computers and EB firmware revisions used in the respective measurements, as explained above.

	f_r (not writing)	f_r (writing)	$t_{\text{dead,wo}}$
`drs_exam_modif_cast_bin_2` as in [9]	100 Hz	79 Hz	2 658 μs
`drs_speedtest` as in this work	535 Hz	525 Hz	36 μs

These findings are a strong indication that a more powerful computer than the GuruPlug should be used for the engineering array.

Optimization: Avoiding repeated time array readout. A typical DRS4 EB event comprises 1024 values of cell data for each of its four channels. In the representation of an event, this cell data populates the y axis, while the 1024 values of time calibration data go on the x axis (see section 3.3 on page 32 for details on time calibration). However, the time calibration data changes only when the board is re-calibrated, and it is sensible to assume that readout is always interrupted for calibration. Thus, the time calibration data are always identical for a large number of consecutive events.

While `drs_exam` reads time calibration data from the EB with every event and writes it as part of every event's data, `drs_speedtest` reads the time array only once per execution and writes it only once per output file. Besides increasing the readout frequency, it also reduces the output file size by $\sim 20\,\%$.

Optimization: Avoiding `short int` casts. The software library provided with the DRS4 EB outputs cell data as `float`-type numbers of large range and precision. But in fact, the cell data actually stored by the software library has a finite precision of 0.1 mV, in accordance with the DRS4 chip's nominal cell precision limit (see section 3.1 on page 29). Given the dynamic range of 1 V, there are only 10 000 distinct possible readout values.

Concerning data volume, the usage of `float`-type numbers is inefficient. A `float` takes up 32 bits of memory to provide decimal fractions with a very large range, whereas 10 000 distinct values can just as well be stored in a `short int`-type number that uses 16 bits of memory to represent up to 65 535 distinct integer values. Storing the cell data as `short int`-type numbers thus reduces the data volume by a factor of 2.

The conversion from `float` to `short int`, however, requires a certain amount of processing time. This tradeoff between processing time and data volume can lead to different results on different systems: on the GuruPlug used in [9], using `short int`-type numbers significantly increased performance, while the opposite was the case on the Office PC used in this work. This was because data writeout was the bottleneck on

Table 6: Data volume per event and relative processing speed of different data types for DRS4 EB readout in [9] and in this work. The ASCII volume is an estimation based on an average of 3.5 leading numerals (including sign), a decimal point and one decimal place.

		relative performance	
data type	event size	GuruPlug	Office PC
`short int`	8 KiB	fastest	fast
`float`	16 KiB	fast	fastest
literal ASCII	22 KiB	slow	slow

the GuruPlug, whereas number conversion was a bottleneck on the Office PC. Table 6 on the previous page gives an overview of these effects.

5.3. Data volume

The data volume produced at high readout frequencies is quite large, as detailed in Table 7. Care has to be taken so that data transfer and/or storage has sufficient capacity and does not pose a bottleneck to the H$_i$SCORE experiment.

In order to avoid diverging memory usage and problems with very large file sizes, `drs_speedtest` allows specifying a maximum number of events to be written to one file. After recording this number of events, the writeout file is closed and another one is opened, assigning sequential file numbers. Events are numbered with a `long int`, which is maintained over all output files.[†]

Appendix C.1 on page 77 lays out the bytewise structure of a data file produced by `drs_speedtest`. As is the case with all custom binary data formats, no existing software can natively handle it.

A very common way of importing and exporting data for maximum compatibility is a CSV file in ASCII format. A tool called `drs_speedtest_binexplode` was written to export data from `drs_speedtest`'s binary format to space-separated ASCII data, using separate files for each event. The source code is shown in Appendix B.2 on page 75.

Table 7: Data volume produced by `drs_speedtest` at different readout frequencies and using different data types for cell data storage. Note that the actual $f_{\max}$ for the `short int` storage variant was measured at 495 Hz.

	data volume per second		data volume per hour	
trigger frequency	`float`	`short int`	`float`	`short int`
100 Hz	1.6 MiB	800 kiB	5.5 GiB	2.8 GiB
200 Hz	3.1 MiB	1.6 MiB	11.0 GiB	5.5 GiB
500 Hz	7.8 MiB	3.9 MiB	27.5 GiB	13.8 GiB

[†]This numbering would only overflow after 47.3 days of uninterrupted operation at the maximum readout frequency of 525 Hz.

Part III.
Prototyping an analog time tagging system

You may be confused about the passage of time.

—GLaDOS

from *Portal 2*,
Valve Corporation (2011)

6. System design and components

Short summary: An analog time-tagging system integrated with the H$_i$SCORE data flow was drafted and tailored to DRS4 readout. A unit called the Clock interpolates 1 pulse per second signals from an external timing source and is sampled along with readout data. From its signal, a timestamp with nanosecond precision can be reconstructed.

6.1. Data stream

For the timing precision of ~ 1 ns aimed at with H$_i$SCORE, cable delays are significant even for cables with lengths of 1 m and less. As the stations will be separated by distances on the order of 100 m, timing either has to be kept locally in each station or distributed by systems designed for remote high-precision timing. One such timing distribution system is White Rabbit [31], which is being tested for use in H$_i$SCORE. This work focuses on a model for a local timing system.

Since the H$_i$SCORE Prototype Array will not feature custom-designed FPGA readout electronics, the data stream from the DRS4 Evaluation Board to the readout computer cannot be expanded to include additional digital information like timing or the status of readout equipment.

As a result of this limitation, timing information has to be gathered in one of two ways: Either by reading it from outside the data stream (e.g. using a GPS receiver connected directly to the readout computer), or by including it in the data stream (i.e. the channel readout), as suggested by the developer of the DRS4 chip in [41, p. 9].

The *Global Positioning System* (GPS) is a satellite navigation system in world-wide operation since 1994. It can be used for timing applications as well as navigation: commercial GPS receivers are capable of high-precision timing with relative errors of below 50 ns between nearby receivers [48]. For such timing applications, the location of the receiver must be known very accurately. This can be achieved by averaging a position measurement over some time before switching to time measurement. Higher precision, down to below 10 ns, is possible where ground-based *GPS augmentation* systems are available [14]. However, such systems are currently available only in North America (WAAS), Europe (EGNOS) and Japan (MSAS), and therefore none of the prospective H$_i$SCORE sites will be able to make use of it (see section 2.3 on page 21).

Also, there would be difficulties timing H$_i$SCORE events with a GPS receiver connected to the readout computer. Most commercial GPS modules provide only a 1 pulse per second (*PPS*) signal. The signal is given at the top of every second with high precision, but to time an event at an arbitrary moment in time, the PPS signal has to be interpolated. The most obvious way to do this is to connect a high-precision oscillator to a counter that is reset with each PPS pulse. When triggered, its counter value is read out and, using the oscillator's frequency, correlated with absolute time. Since reading out a digital counter would require custom FPGA hardware, it is not an option for the H$_i$SCORE Prototype Array.

If the GPS receiver has a feature that allows it to be triggered and then give out absolute time with high precision, it has to be ensured that GPS time readout is triggered at exactly the same instant as data readout. GPS receivers are typically connected to a PC via RS-232 serial connections or USB connections. USB data connections have an inherent granularity of 1 ms (see section 5.1 on page 43), while the maximum data rate of 115.2 kilobaud[†] for RS-232 connections implies a granularity of at least 8.7 μs. This necessitates *push readout*, where the computer waits for the device to transmit an event once it has been triggered, as opposed to the computer requesting an event at a certain time (*pull readout*). Even so, the readout frequency will be limited by the data connection's time granularity, rendering the setup unfit for readout frequencies substantially higher than the $\sim$500 Hz limit of the DRS4 EB.

This work focuses on integrating timing information into the DRS4's data stream. To this end, the output of a device called *Clock* is sampled in two or more of the DRS4's channels, from which absolute time can be reconstructed offline.

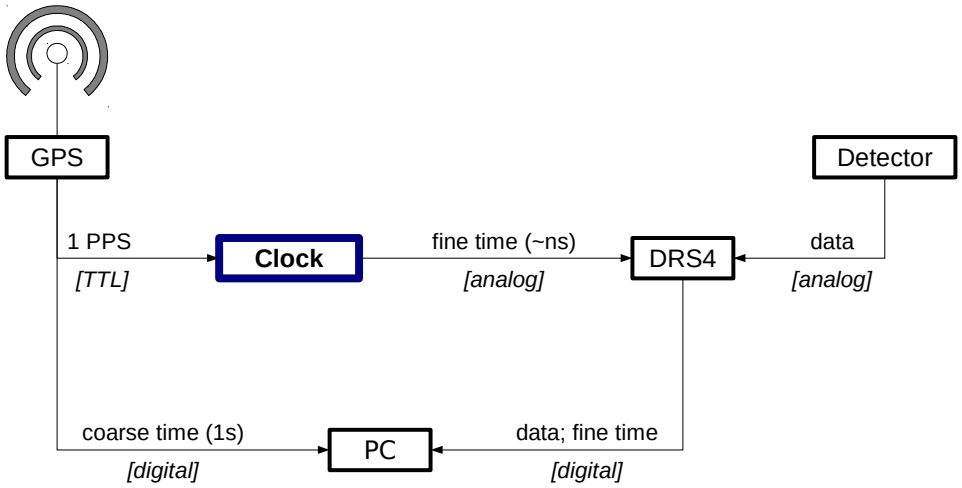

Figure 29: Schematic overview of the time tagging system proposed.

In the proposed system, time information is split into two parts, which are treated separately: The *date* down to the current second (also called *coarse time*) and sub-second time information that should be exact down to 1 ns (also called *fine time*).

Coarse time is provided by a GPS receiver connected to the readout computer. It provides the current date and time of day and is supposed to ensure that for events read out by the computer, the corresponding file is marked with the current absolute time accurate to the second. This is important to keep track of which portion of the

[†]Baud is a unit for data transfer speed. It is defined as *symbols per second*. For ASCII data, where one symbol is equivalent to eight bits, 1 baud $\widehat{=}$ 8 bytes/s.

sky was in view at the time an event was recorded, and in order to keep track of possible time-dependent variations signals from celestial sources.

The GPS receiver also resets the Clock, which interpolates PPS pulses with an accuracy of 1 ns. Because this way the fine time uses the coarse time as a reference, *the timing accuracy of this system for measurements across different H_iSCORE stations is limited by the relative accuracy of the coarse time in the respective stations.* A remedial measure is to ensure that all GPS receivers always use the same satellites at any given time. Given that the H_iSCORE stations are co-located with respect to celestial visibility, this should not pose any problems.

To circumvent this limitation entirely, a higher-precision PPS source can be used, like a radio signal or light pulse distributed over the entire array. It can provide better accuracy, provided that the location-dependent absolute offset due to light run time ($\sim$33 ns for 10 m) and any drift between GPS time and the PPS source are corrected for.

6.2. The Clock

The Clock interpolates time between two PPS pulses with an accuracy of 1 ns and continuously outputs this information as an analog signal.

For use with the DRS4 chip, the signal must convey this information in the time called the *readout window*: It is given by $t_s = 1024 \cdot f_s^{-1}$ since the DRS4 chip has a buffer that is 1024 cells deep. Also, no more than the DRS4's dynamic range of 1 V can be used. This work assumes a readout frequency of $f_s = 1\,\text{GHz}$, where $t_s \approx 1\,\mu\text{s}$.

Ramp signals of constant slope are the central element of the Clock. They reset with each PPS pulse to stay in phase with coarse time as outlined above. A ramp signal with frequency $f_r = 1\,\text{Hz}$ has a slope of $S = 1\,\frac{\text{V}}{\text{s}}$ and rises from 0 V to 1 V in 1 second. If it is sampled at any time Δt after the last PPS pulse, the voltage will read $U_r = S \cdot \Delta t$: At 0.2 s after the last reset, it will read 200 mV.

Consider Fig. 30 on the next page. The top graph shows a ramp with $f_r = 1\,Hz$. The bottom left graph shows the readout window for that ramp when read out at the time of the trigger ($\sim$ 370 ms in this example). The trigger time is indicated by the red vertical line in the top graph. Note that in the readout window, the slope of $0.001\,\frac{\text{mV}}{\mu\text{s}}$ is undetectable.

Now consider a second ramp of higher frequency, say $f_r = 10\,\text{Hz}$. If it is still reset once every second, then any readout value has a ten-fold *ambiguity*: $U_r = 720\,\text{mV}$ could correspond to any Δt in $\{72\,\text{ms}, 172\,\text{ms}, 272\,\text{ms}, \ldots, 972\,\text{ms}\}$. In the example in Fig. 30, the middle graph shows such a ramp. The bottom right graph shows its readout window, when triggered at the same time as the $f_r = 1\,\text{Hz}$ ramp. The ambiguity of the second ramp's readout is then resolved by the readout of the first ramp: Since $U_{r,1\text{Hz}} \approx 370\,\text{mV}$, the readout of $U_{r,10\text{Hz}} \approx 720\,\text{mV}$ corresponds to $\Delta t = 372.0\,\text{ms}$.

The DRS4 EB's nominal cell readout noise of 0.35 mV theoretically allows for an ac-

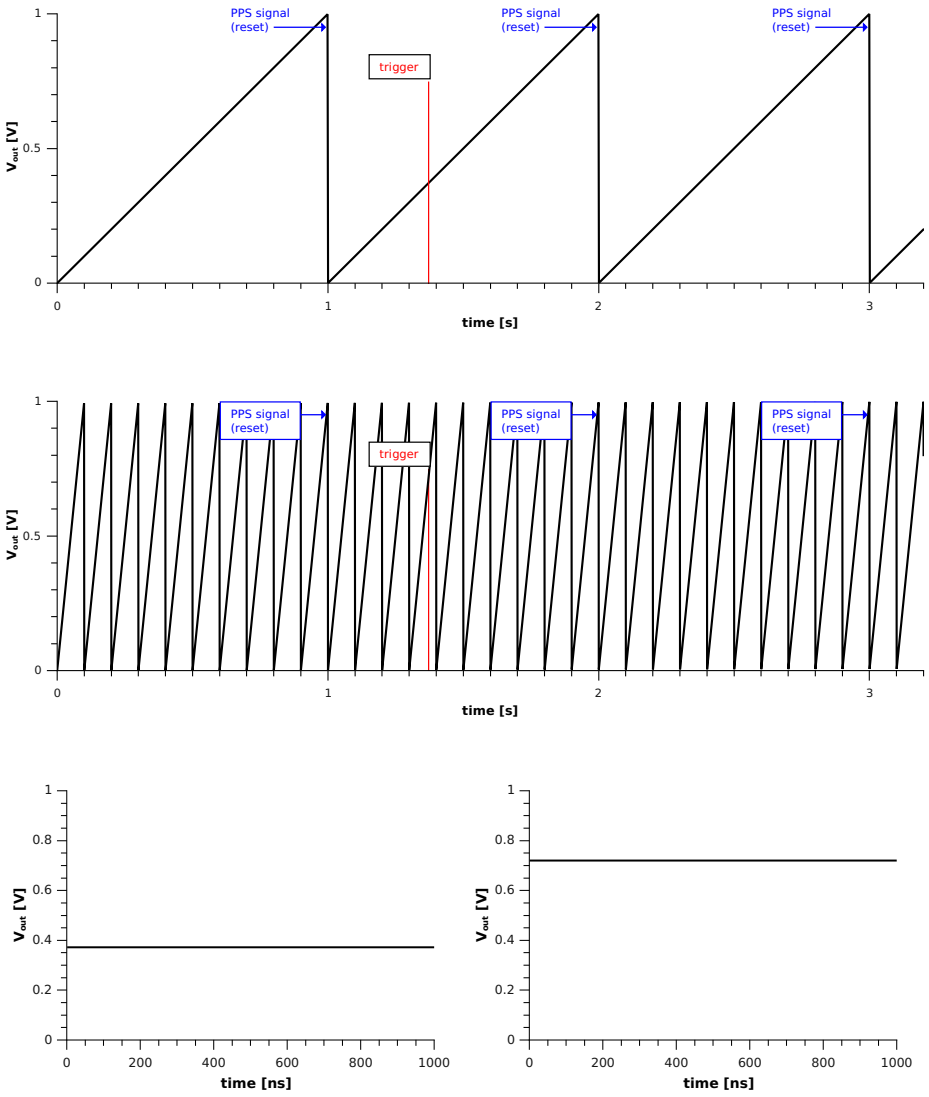

Figure 30: Graphs illustrating the working principle of the Clock. A trigger at 372 ms after reset is indicated. **Top:** 1 Hz ramp. **Middle:** 10 Hz ramp.
Bottom left: Readout window of the 1 Hz ramp at trigger time. **Bottom right:** Readout window of the 10 Hz ramp at trigger time.
Note that the readout windows for both ramps show constant signals, because the slope is too small to be detected over $\sim 1\,\mu$s.

curacy of 1 ms in Δt to be expected for the $f_r = 1\,\mathrm{Hz}$ ramp. With a second ramp of $f_r = 1\,\mathrm{kHz}$, a combined accuracy of $1\,\mu\mathrm{s}$ in Δt can be achieved.

In general, two or more ramps sampled in correspondingly many channels of a readout device can provide PPS interpolation timing according to this principle. The frequencies and the resulting timing precision are dependent on the accuracy/jitter of the readout. The system described so far would also work with momentary, single-value readout as opposed to a readout window.

Further improved precision can be achieved if a sine signal of small amplitude is added to the ramps and fitted for phase. For good fitting, the frequency needs to be high enough for several periods to fall within the readout window. The absolute offset corresponds to the ramp level, the phase fit provides further timing precision. See Fig. 31 for an illustration of such a signal. This procedure only makes sense if the precision of the ramps alone is sufficient to resolve the large ambiguity of the sine signal.

Adding sine signals to the ramps has the advantage of adding precision to the system without the need for more channels. This is desirable given the DRS4 EBs limited number of four input channels. If, however, the number of input channels is not an issue, a simpler system with a larger number of plain ramps can be preferable.

For the DRS4 EB, taking into account the nominal jitter of 0.35 mV per cell and assigning ramps augmented with sine signals of frequencies from 1 to 5 MHz to two input channels, an overall combined accuracy of 1 ns can plausibly be achieved.

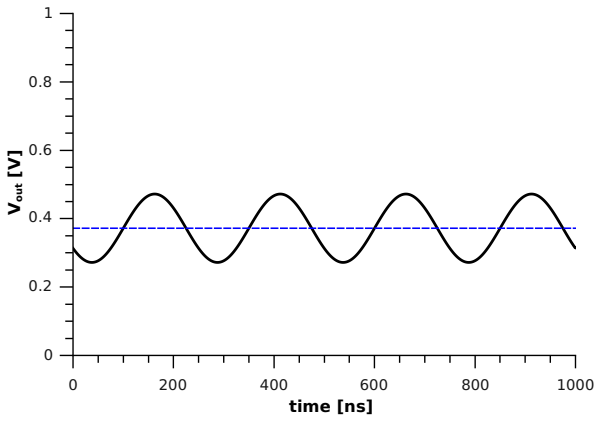

Figure 31: A graph illustrating the readout window of a ramp overlayed with a high-frequency sine signal. The ramp offset of $\sim 370\,\mathrm{ms}$ is indicated by the blue dashed line. The added sine signal has a period of $250\,\mathrm{ns} = 4\,\mathrm{MHz}^{-1}$ and in this readout window exhibits a phase offset of 150 ns since the last full period.

7. Simulation and emulation of the Clock

Short summary: The Clock was simulated and tested with reconstruction software written for the proposed system. The simulations show the system to be viable with DRS4 readout hardware in principle. However, emulating the Clock with off-the-shelf function generator hardware and testing it with a DRS4 Evaluation Board failed for lack of precision on the part of the function generators.

7.1. Simulation

For simulation, software was written to emulate the output of the Clock. The output is computed directly from analytical functions, without simulating electronic components. A normally distributed jitter of $\sigma = 4\,\mathrm{mV}$ is added independently for each cell. See Fig. 32 for a signal generated by this simulation.

Fitting and analysis of the simulated signals was performed with an independently written piece of software that was used later for analysis of the hardware-generated signals with only minimal adaptations. Its source code is given in Appendix B.3 on page 76.

The simulation was successful in that it achieved sub-nanosecond precision with two ramps of $f_r = 1\,\mathrm{Hz}$ and $f_r = 1\,\mathrm{kHz}$ as well as one 5MHz sine signal added to one of the ramps, as presented above.

Later hardware emulation of the Clock with off-the-shelf devices and its analysis with similar software failed to even fit a 1 Hz ramp with an accuracy of 1 ms. Therefore, the simulation must be said to be much too optimistic about the signal quality of the Clock and the precision of the readout.

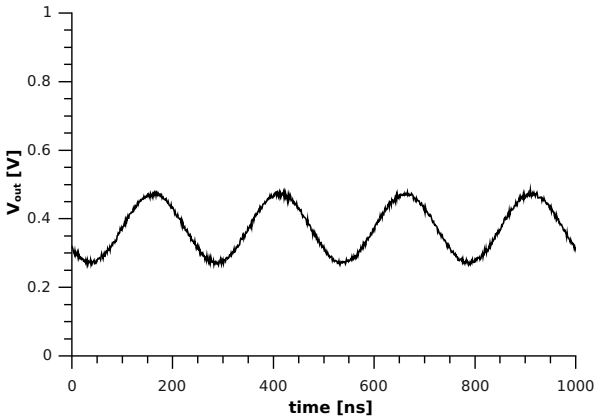

Figure 32: A graph showing a readout window of a ramp overlayed with a high-frequency sine signal as generated by the simulation software written to emulate the Clock. The time since the last reset is identical to that shown in Fig. 31 on the previous page (372 ms + 150 ns).

7.2. Hardware requirements

In the time taken for this work, no resources were available for development and production of a Clock as specified above. Nevertheless, requirements for an implementation were established, which are detailed in section 7.2.

Subsequently, the Clock was emulated using off-the-shelf function generator hardware and read out with a DRS4 EB. An oscilloscope was used to take reference readings for comparison.

As the Clock's signals need to be of very high precision, the electronic parts used to implement it must be very accurate. Most circuits used to generate ramp signals make use of a current source and capacitors. A true current source for the relatively small dynamic range of 1 V and ceramic capacitors with EIA Class 1 dielectrics could provide the necessary linearity. If potentiometers are to be used, e.g. for calibration, they should be digital ones that do not suffer from the wear and drag of their mechanical counterparts.

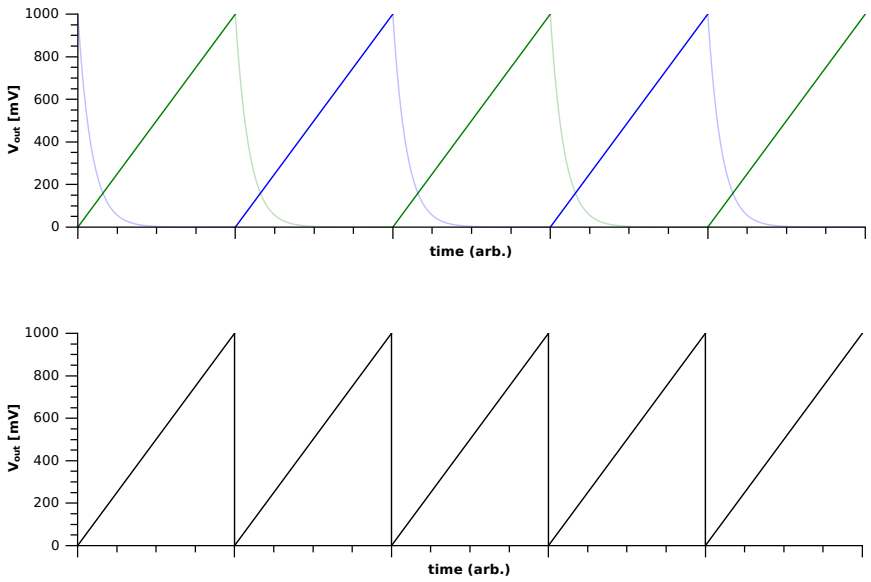

Figure 33: Graphs illustrating the switching of capacitors for continuous sawtooth signal generation. **Top:** Output signals of two capacitors (blue and green curves) alternately charging and discharging, with a phase offset of 180°. The charging flanks are highlighted. **Bottom:** The resulting signal if output is continuously switched to only reflect the charging flanks.

The reset of the ramp cannot happen instantly if the signal is to be generated with a capacitor. The discharge time has to be much smaller than the readout window, so that the falling signal cannot be mistaken for a regular rising signal. To avoid

the sampling of falling signals altogether, several capacitors could be charged and discharged simultaneously, with the output switched to a fully discharged capacitor upon ramp reset. Figure 33 on the previous page illustrates this concept. This option is, however, only useful if the switching between subcircuits causes acceptably little signal distortion.

In order to ensure accurate synchronization between the PPS signal and the ramps, a phase-locked loop (PLL) can be used. Such a system would probably be necessary to stabilize the higher-frequency ramps of the Clock and ensure its phase lock with the PPS signal. Phase-locked loops are delicate circuits and always subject to jitter themselves [13]. Often, PLLs are operated in a thermally stabilized environment to mitigate temperature-dependent drifts. This poses a challenge to their fitness for use in H$_i$SCORE stations, which are likely to be operated at sites with large temperature differences.

7.3. Hardware emulation

When setting up function generators to emulate the Clock, it was found that low-frequency ramps (up to roughly 30 kHz) cannot be read out with the DRS4 EB. This is because the DRS4 EB's inputs are AC coupled, functioning as a high-pass filter for the reduction of low-frequency noise such as power supply interference [42, p. 5]. Therefore, it is not possible to use a Clock with low-frequency ramps as described above with the DRS4 EB.

In order to maintain the basic principle of the Clock, it was decided to modulate the amplitude information onto a high-frequency sine signal, as illustrated in Fig. 35 on page 58. If an adequate frequency is chosen, it can serve not only as a carrier, but also for phase measurement and timing refinement as introduced with Fig. 31 on page 53.

With amplitude modulation, the *modulation depth* is an important parameter. It describes the maximum amplitude change of the output signal in terms of the amplitude of the unmodulated carrier signal. See Fig. 35 on page 58 for an illustration: the unmodulated signal has a peak-to-peak amplitude of 500 mV. At 100 % modulation depth, the variation is (500 ± 500) mV, resulting in a peak-to-peak amplitude range of 0–1000 mV for the modulated signal. At 50 % modulation depth, the variation is (500 ± 250) mV, resulting in a peak-to-peak amplitude range of 250–750 mV. See the description of the setup on page 59 for details on which modulation depth was used.

Three function generators and one oscilloscope were used alongside the DRS4 EB for emulation and testing of the Clock's working principle.

Two modern function generators were used[†] along with one very old Philips device with a unique feature: a manual switch that allows triggering a single pulse output by hand. This Philips device is referred to as the *pulse generator* hereinafter.

In the test setup as shown in Fig. 34 on the following page, the internal amplitude

[†]The Textronix is a two-channel model AFG3252, while the HP is a one-channel model 33120A. Both were no more than five years old.

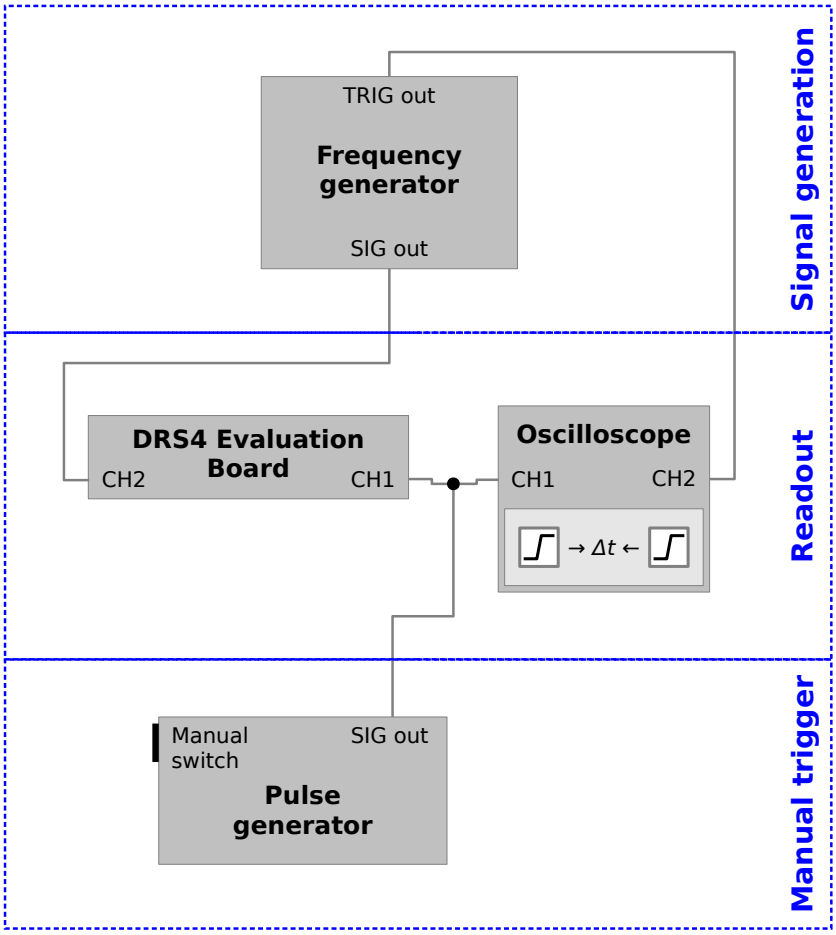

Figure 34: Schematic of the setup used in testing the Clock emulation. The function generator (the Tektronix or the HP in setups 1 and 2, respectively) outputs the Clock signals, while the DRS4 EB samples the Clock when triggered by the pulse generator. The oscilloscope provides a reference reading by relating this trigger to the time elapsed since the last PPS from the function generator.

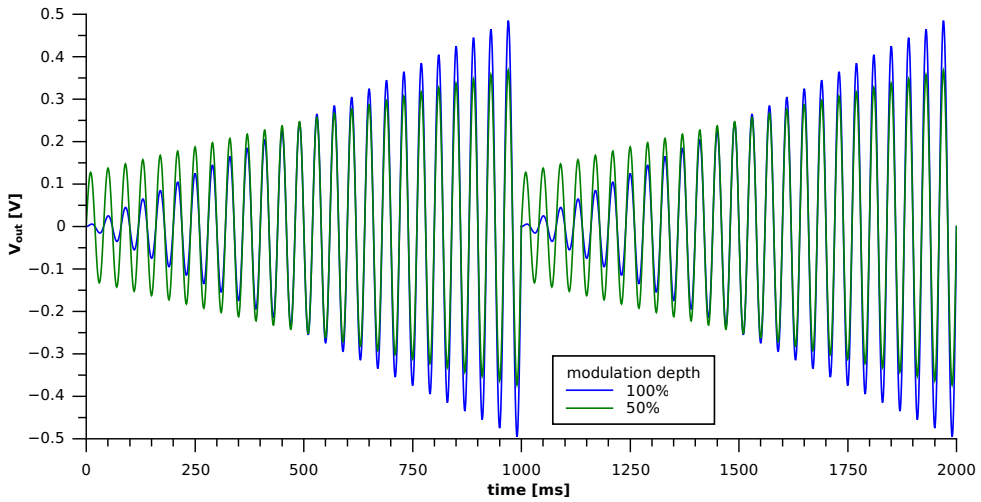

Figure 35: Illustrations of a ramp with $f_r = 1\,\text{Hz}$ amplitude modulated onto sine carrier signals with different modulation depths. The carrier frequency as depicted for visibility is 25 Hz. In testing, a carrier frequency of 5 MHz was used.

modulation feature of the function generator is used to generate the 5 MHz carrier modulated with a 1 Hz signal. The oscilloscope is connected to the *trigger output* of the function generator, which outputs a rectangular pulse with every cycle, i.e. at the top of every second, effectively emulating the PPS signal. This setup was tested with both function generators, the Tektronix in *setup 1* and the HP in *setup 2*.

DRS4 EB Readout is triggered manually using the switch on the Philips pulse generator. Additionally, the oscilloscope is set to compute the time difference between the last emulated PPS from the function generator and this manual trigger, providing a reference measurement to compare with the fit of the Clock output. Ideally, both the oscilloscope and the Clock fit would give the same amount of time passed between the last PPS and the toggling of the trigger.

Table 8: Amplitude modulation parameters for the two setups used in Clock emulation. Values marked with * are approximate and reconstructed from the calibration data. They are not necessarily identical to those actually programmed into the function generators.

setup	modulated amplitude min / max	unmodulated amplitude*	modulation depth*
1: Tektronix AFG3252	32.3 mV / 903.9 mV	468 mV	93 %
2: HP 33120A	147.3 mV / 984.3 mV	565 mV	74 %

With both function generators, large discrepancies were seen between the expected signal shape according to the modulation parameters and the actually measured signal. For example, the Tektronix function generator exhibited high-frequency harmonic noise (estimated at about 200 MHz) for small amplitudes that hindered fitting. The HP function generator also showed a distorted signal at small amplitudes. In order to counteract these effects, modulation parameters were tuned for signal quality, which included choosing modulation depths smaller than 100 % and unmodulated base amplitudes other than 500 mV. For an overview of the settings used, see Table 8 on the previous page.

Therefore, the time-amplitude correlation of the two setups was not well-defined, and had to be manually calibrated. For this purpose, the modulating signal was switched from a ramp to a square and the modulated output signal's maximum and minimum amplitudes measured by averaging over many cycles. Still, a linear time-amplitude correlation was assumed between the values calibrated to be the minimum ($\widehat{=}$ 0 ms) and maximum ($\widehat{=}$ 1000 ms) amplitudes (which, in light of the disappointing results, might not be accurate).

7.4. Measurement and results

Figure 36 on the following page shows a Clock timestamp recorded with setup 2 as described above. Ten such events were recorded with setup 1, fifteen with setup 2. They were evaluated by fitting the signals and reconstructing the encoded timestamp under the assumption that the function generator's output conformed to the specifications of the Clock.

The software used for these calculations is given in Appendix B.3 on page 76. It assumes a fixed frequency of 5 MHz for the Clock signal and fits a sine function for an additive offset, phase offset and amplitude. From the amplitude fit, the corresponding time since the last PPS is calculated, taking into account the signal calibration as described in the previous section.

Unfortunately, none of the tests yielded the expected accuracy. Instead, large deviations were seen with little or no apparent systematic shifts that could readily be corrected for. After it was established that the available hardware would not work as expected with the 1 Hz ramp, no higher-frequency ramps or phase fits were investigated.

See Table 9 on page 62 for an overview of the results of tests with the 1 Hz ramp for both setups. The seeming bias towards times between 600 ms and 900 ms after the PPS (where 15 out of 25 events fell) is incidental.

It is obvious that deviations between the fit values and the oscilloscope readings are systematic and large. Most likely, they are due to poor signal quality, as illustrated in Fig. 37 on page 61. Deviations of this type and magnitude were seen in nearly all recorded events. Deviations are larger for smaller amplitudes (corresponding to shorter times after the PPS). This is consistent with the observations of noise and signal distortions at small amplitudes described in the previous section. Because of

the poor signal quality, and because the oscilloscope's reference reading does not use the Clock signal, but rather just compares rectangular trigger pulses, it can safely be assumed that the oscilloscope gives the true (or, at least, much more precise) time difference between the trigger time and the last PPS.

An overview of the fitted timestamps and their deviation from the oscilloscope reference data is given in Fig. 38 on page 62. Apparently, deviations are indeed systematically larger at smaller amplitudes. The data for setup 1 appear to follow a linear correlation of roughly 0.8 ns of deviation per 100 ms ($\widehat{=}$ 87 mV in amplitude for setup 1), but even if corrected for this unexplained effect, the data still shows deviations of more than 1 ms. The data for setup 2 appear to be correlated in a similar way, but much less strongly, and deviations are larger overall and spread further.

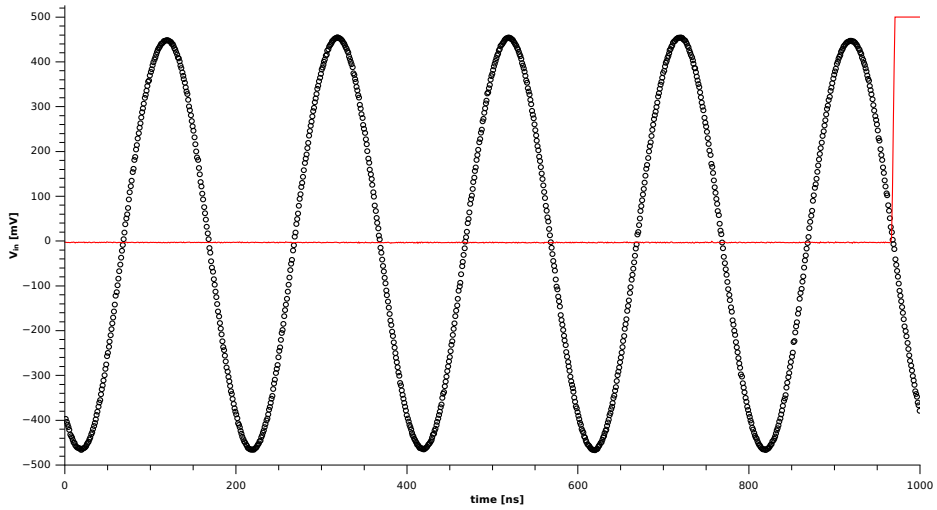

Figure 36: Overview of the Clock timestamp sampled by the DRS4 EB along with the trigger channel (red).

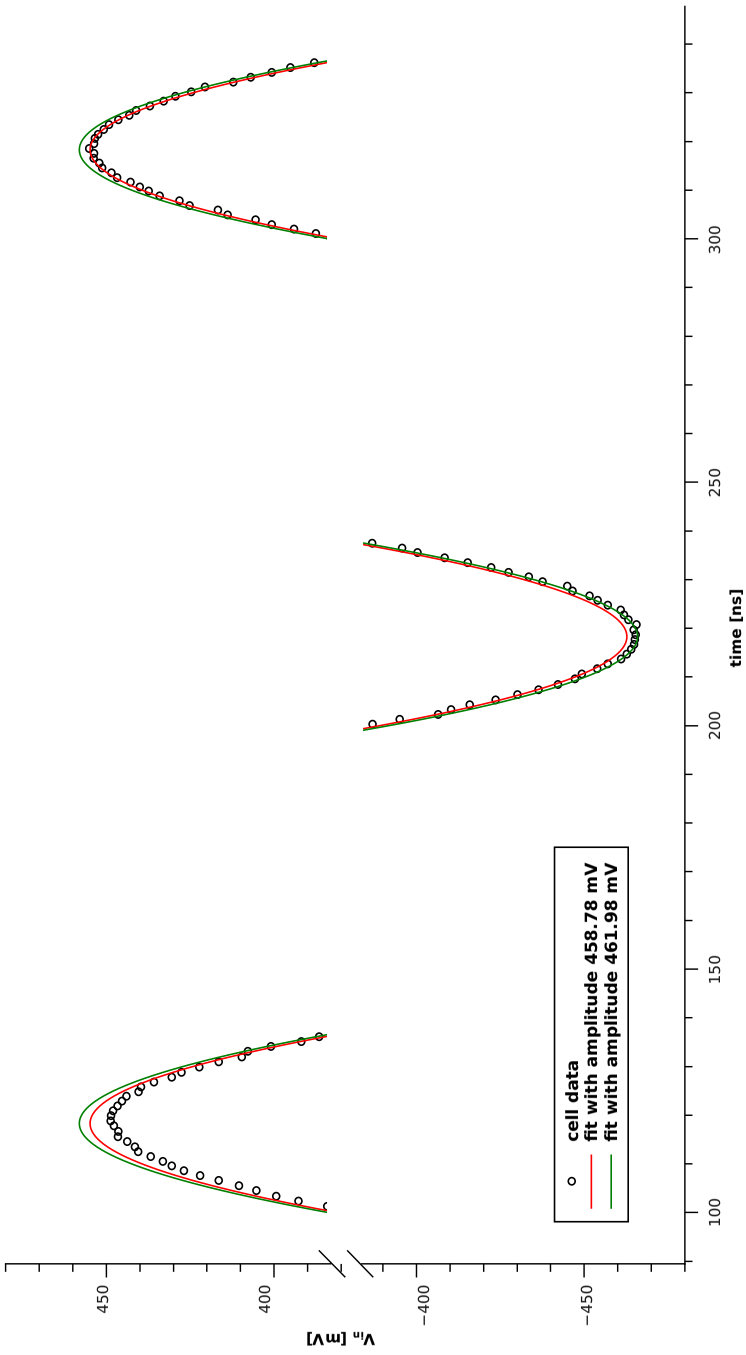

Figure 37: Detailed view of selected parts of the event shown in Fig. 36 on the previous page, along with two fit functions that differ only in their amplitude parameter (red and green). Note how both fit functions fail to coincide with the data points in different parts of the curve, indicating inferior signal quality.

Table 9: Oscilloscope readings and fit results for events recorded from the emulated Clock for both setups. Events were triggered manually at no particular times. A graphical overview of the calculated deviations is given in Fig. 38.

setup 1			setup 2		
oscilloscope	fit	difference	oscilloscope	fit	difference
98.7 ms	89.1 ms	9.6 ms	51.3 ms	40.0 ms	11.3 ms
358.7 ms	351.3 ms	7.4 ms	80.9 ms	69.7 ms	11.2 ms
390.4 ms	383.3 ms	7.1 ms	469.6 ms	466.2 ms	3.4 ms
391.8 ms	384.9 ms	6.9 ms	500.7 ms	490.3 ms	10.4 ms
451.8 ms	445.6 ms	6.2 ms	718.1 ms	711.6 ms	6.5 ms
610.3 ms	605.4 ms	4.9 ms	731.5 ms	730.1 ms	1.4 ms
652.9 ms	648.2 ms	4.7 ms	777.2 ms	772.3 ms	4.9 ms
662.4 ms	657.7 ms	4.7 ms	759.9 ms	758.5 ms	1.4 ms
675.3 ms	670.1 ms	5.2 ms	797.8 ms	799.0 ms	-1.2 ms
897.8 ms	893.7 ms	4.1 ms	812.9 ms	810.3 ms	2.6 ms
			813.8 ms	814.4 ms	-0.6 ms
			823.1 ms	818.3 ms	4.8 ms
			828.2 ms	824.3 ms	3.9 ms
			877.4 ms	873.9 ms	3.5 ms
			927.9 ms	920.3 ms	7.6 ms

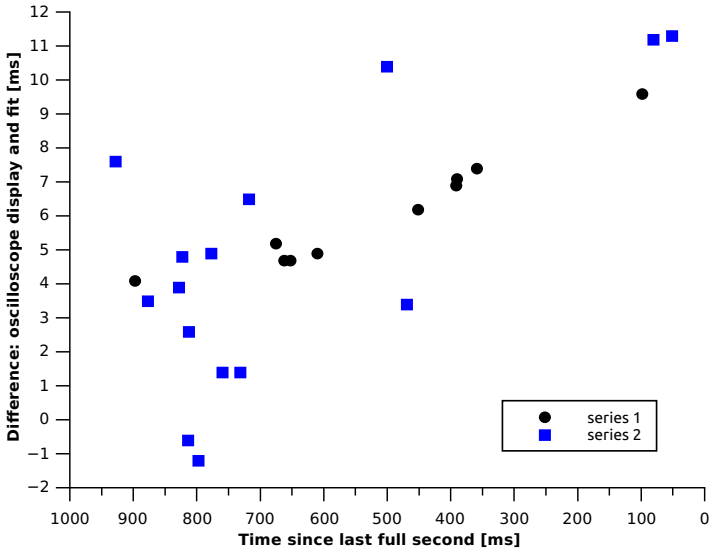

Figure 38: Deviations between Clock timestamp fits and oscilloscope reference readings for both setups. Note the inverse scale on the horizontal axis.

Part IV.
Conclusions and outlook

But there's no sense crying
over every mistake.
You just keep on trying
till you run out of cake.

—GLaDOS

---

from *Portal*,
Valve Corporation (2007)

8. Data readout in H$_i$SCORE stations

The DRS4 chip is a data acquisition device that is well-suited for the H$_i$SCORE detector. Its high sampling rate and timing accuracy provide the necessary precision for γ-ray observation.

The DRS4 Evaluation Board is adequate for Prototype Array operations. Systematic and random errors in timing synchronization between the four different input channels are well below 1 ns. The USB connection for data readout allows for a maximum trigger frequency of about 520 Hz, but a powerful enough computer is needed. The GuruPlug PC proved to be a serious bottleneck for readout speed, and must therefore be said to be inadequate for H$_i$SCORE. Instead, a common office PC may be the right device for H$_i$SCORE stations: it has sufficient computing power for readout and enough memory and storage to deal with large data volumes, it can provide faster and more stable data connection ports as well as (more or less well regulated) power and even, to a certain degree, heating.

In light of the limitation to USB readout and four input channels in the DRS4 Evaluation Board, a custom H$_i$SCORE readout board for the DRS4 chip is preferable for the Engineering Array. For the development of this board, several aspects relevant to timing must be taken into account:

- The signal pathways for different channels should differ as little as possible in length and surrounding conditions (like the proximity to power supply lines or geometric layout). Although absolute offsets can be calibrated for, widely differing conditions for different input channels unnecessarily complicate reconstruction.
- The data connection should be substantially faster than the request/response USB readout implemented in the DRS4 Evaluation Board V3. The ADC/dead time tradeoff should be considered if it could make a difference given the prospective data connection.
- The board should provide convenient self-calibration measures. Both a high-precision oscillator and a high-bit DAC should be present for timing and voltage calibration. It is possible to have the oscillator permanently connected to an input channel and sample it with every event, allowing per-event time calibration, an ideal method to counteract any drifts in aperture jitter.
- In order to prevent the domino stop time effect from introducing a random timing uncertainty of 2 to 3 ns for the time between a trigger and the actual readout, the trigger signal has to be sampled on the same chip as is being triggered. This also means that if several chips are to be used on the board, the original trigger signal has to be distributed to all of them.
- A temperature sensor can allow for temperature-dependent calibration of noise and/or jitter, if such a dependency is found.

For ideal timing precision, then, two of the nine channels of the DRS4 chip are reserved for time calibration and trigger sampling. Given that there are four photomultipliers

and very probably an external time synchronization signal, it is likely that the readout board will require at least two DRS4 chips to accommodate all signals.

Under all circumstances should the design of the readout board be discussed with the developers of the DRS4 chip, as their insight and experience with the development of DRS4-related readout hardware is unmatched.

9. Time synchronization between H$_i$SCORE stations

For the Prototype Array deployed at the TUNKA site, there have been very promising trials of the Ethernet-based White Rabbit time synchronization system [49].

The system described in this work can be a wireless alternative or a means of cross-checking time synchronization. Its working principle is viable with DRS4 readout hardware, but extensive hardware development is necessary for an implementation of the Clock.

Furthermore, its precision with respect to absolute time is dependent on the precision of a master signal. In this work, the GPS system was assumed to provide that master signal, but in reality it cannot be expected to ever yield an accuracy greater than 10 ns.

However, nanosecond time synchronization that is faithful to absolute time is secondary for the purposes of H$_i$SCORE. Any system that provides *relative* timing with sufficient precision would suffice. Coarse time can always be obtained from a different system like GPS, or distributed through a computer network.

In [16], a radio beacon system like that of the LOPES detector is suggested for this purpose. However, that system only gathers data on the *change* of the relative timing offset between stations. It has revealed an extreme sensitivity of the radio signal's propagation to the geometric layout and environmental conditions of the array. Season-dependent drifts on the order of several nanoseconds were found, which are not yet understood [43].

Nevertheless, its principle might be adapted with visible light instead of radio signals. Given that the location of the sender and the stations is known with a precision of no worse than several centimeters (in order to calibrate for the arrival time delay), and that environmental conditions do not impede or distort the signals, a high-precision time reference signal could be broadcast in the form of visible light pulses. This signal could then be interpolated by the system described in this work to provide a high-precision time stamp in the data stream.

Further investigation and effort towards wireless time synchronization is definitely warranted in light of the far greater material requirements of a cable-based system for the final H$_i$SCORE array.

Part V.
Appendix

A. References

[1] Analog Devices, *14-Bit, 20 MSPS/40 MSPS/65 MSPS/80 MSPS, 3 V A/D Converter AD9245*, datasheet, 2006,
http://www.analog.com/static/imported-files/data_sheets/AD9245.pdf.

[2] Aya Bamba, Ryo Yamazaki, Masaru Ueno, and Katsuji Koyama, *Small-Scale Structure of the SN 1006 Shock with Chandra Observations*, The Astrophysical Journal **589** (2003), no. 2, 827,
SAO/NASA ADS: http://adsabs.harvard.edu/abs/2003ApJ...589..827B.

[3] J. Blümer, R. Engel, and J. R. Hörandel, *Cosmic rays from the knee to the highest energies*, Progress in Particle and Nuclear Physics **63** (2009), 293–338,
SAO/NASA ADS: http://adsabs.harvard.edu/abs/2009PrPNP..63..293B
arXiv: http://arxiv.org/abs/0904.0725.

[4] J. van Buren, *Investigations of the Muon Component of Extensive Air Showers Measured by KASCADE-Grande*, Ph.D. thesis, Universität Karlsruhe (TH), now Karlsruhe Institute of Technology (KIT), March 2007,
KIT Library: http://bibliothek.fzk.de/zb/abstracts/7292.htm.

[5] P. Carlson and A. de Angelis, *Nationalism and internationalism in science: the case of the discovery of cosmic rays*, European Physical Journal H **35** (2010), 309–329,
SAO/NASA ADS: http://adsabs.harvard.edu/abs/2010EPJH...35..309C
arXiv: http://arxiv.org/abs/1012.5068.

[6] CODALEMA Collaboration, *Geomagnetic origin of the radio emission from cosmic ray induced air showers observed by CODALEMA*, Astroparticle Physics **31** (2009), 192–200,
SAO/NASA ADS: http://adsabs.harvard.edu/abs/2009APh....31..192A
arXiv: http://arxiv.org/abs/0901.4502.

[7] Compaq, Intel, Microsoft and NEC, *Universal Serial Bus Specification*, Revision 1.1, September 1998.

[8] K. Czuba and D. Sikora, *Temperature Stability of Coaxial Cables*, Acta Physica Polonica A **119** (2011), 553,
CERN Document Server: http://cdsweb.cern.ch/record/1349292.

[9] R. Eichler, *Slow Control und Datenauslese für den H_iSCORE-Detektor*, Diploma thesis, University of Hamburg, February 2011.

[10] R. Engel, D. Heck, and T. Pierog, *Extensive Air Showers and Hadronic Interactions at High Energy*, Annual Review of Nuclear and Particle Science **61** (2011), 467–489,
SAO/NASA ADS: http://adsabs.harvard.edu/abs/2011ARNPS..61..467E.

[11] H. Falcke et al., *Detection and imaging of atmospheric radio flashes from cosmic ray air showers*, Nature **435** (2005), 313–316,
SAO/NASA ADS: http://adsabs.harvard.edu/abs/2005Natur.435..313F

arXiv: http://arxiv.org/abs/astro-ph/0505383.

[12] T. K. Gaisser and A. M. Hillas, *Reliability of the method of constant intensity cuts for reconstructing the average development of vertical showers*, International Cosmic Ray Conference **8** (1977), 353–357,
SAO/NASA ADS: http://adsabs.harvard.edu/abs/1977ICRC....8..353G.

[13] X. Gao, E.A.M. Klumperink, P.F.J. Geraedts, and B. Nauta, *Jitter analysis and a benchmarking figure-of-merit for phase-locked loops*, IEEE Transactions on Circuits and Systems II: Express Briefs **56** (2009), no. 2, 117–121.

[14] L. Gauthier, P. Michel, J. Ventura-Traveset, and J. Benedicto, *EGNOS: the first step in Europe's contribution to the global navigation satellite system*, ESA bulletin **105** (2001), 35–42.

[15] A. Gockel, *Luftelektrische Beobachtungen bei einer Ballonfahrt*, Physikalische Zeitschrift **XII** (1911), 597.

[16] D. Hampf, *Study for the wide-angle air Cherenkov detector HiSCORE and time gradient event reconstruction for the H.E.S.S. experiment*, Ph.D. thesis, Universität Hamburg, May 2012,
Universität Hamburg E-Dissertationen: http://ediss.sub.uni-hamburg.de/volltexte/2012/5699.

[17] D. Hampf, M. Tluczykont, D. Horns, and G. Rowell, *Simulation of expected performance and site evaluation for the proposed gamma-ray detector SCORE*, 38th COSPAR Scientific Assembly, Committee on Space Research (COSPAR) Meeting, vol. 38, 2010,
SAO/NASA ADS: http://adsabs.harvard.edu/abs/2010cosp...38.2338H.

[18] William Hanlon, *William Hanlon's Web Page: Updated Cosmic Ray Spectrum*, 2009, http://www.physics.utah.edu/~whanlon/spectrum.html.

[19] V.F. Hess, *Über Beobachtungen der durchdringenden Strahlung bei sieben Freiballonfahrten*, Physikalische Zeitschrift **XIII** (1912), 1084–1091.

[20] H.E.S.S. Collaboration, *Discovery of Very High Energy γ-Ray Emission from Centaurus a with H.E.S.S.*, The Astrophysical Journal Letters **695** (2009), L40–L44,
SAO/NASA ADS: http://adsabs.harvard.edu/abs/2009ApJ...695L..40A
arXiv: http://arxiv.org/abs/arXiv:0903.1582.

[21] ———, *First detection of VHE γ-rays from SN 1006 by H.E.S.S.*, Astronomy and Astrophysics **516** (2010), A62,
SAO/NASA ADS: http://adsabs.harvard.edu/abs/2010A&A...516A..62A
arXiv: http://arxiv.org/abs/1004.2124.

[22] J. A. Hinton for the H.E.S.S. Collaboration, *The status of the H.E.S.S. project*, "New Astronomy Reviews" **48** (2004), 331–337,
SAO/NASA ADS: http://adsabs.harvard.edu/abs/2004NewAR..48..331H
arXiv: http://arxiv.org/abs/astro-ph/0403052.

[23] A. M. Hillas, *Differences between Gamma-Ray and Hadronic Showers*, Space Science Reviews **75** (1996), 17–30,

SAO/NASA ADS: http://adsabs.harvard.edu/abs/1996SSRv...75...17H.

[24] H$_i$SCORE Collaboration, *H$_i$SCORE Homepage*, http://wwwiexp.desy.de/groups/astroparticle/score/en/.

[25] IceCube Collaboration, *Time-integrated Searches for Point-like Sources of Neutrinos with the 40-string IceCube Detector*, Astrophysics J **732** (2011), 18, SAO/NASA ADS: http://adsabs.harvard.edu/abs/2011ApJ...732...18A arXiv: http://arxiv.org/abs/1012.2137.

[26] Y. Inoue, T. Totani, and M. Mori, *Prospects for a Very High-Energy Blazar Survey by the Next-Generation Cherenkov Telescopes*, Publications of the Astronomical Society of Japan **62** (2010), 1005, SAO/NASA ADS: http://adsabs.harvard.edu/abs/2010PASJ...62.1005I arXiv: http://arxiv.org/abs/1002.4782.

[27] B. Keil, S. Lehner, and Stefan Ritt, *Application of a 5 GSPS Analogue Ring Sampling Chip for Low-cost Single-shot BPM Systems*, 11th European Particle Accelerator Conference, June 2008, CERN Document Server: http://cdsweb.cern.ch/record/1183128.

[28] K. Koyama, R. Petre, E. V. Gotthelf, U. Hwang, M. Matsuura, M. Ozaki, and S. S. Holt, *Evidence for shock acceleration of high-energy electrons in the supernova remnant SN1006*, Nature **378** (1995), 255–258, SAO/NASA ADS: http://adsabs.harvard.edu/abs/1995Natur.378..255K.

[29] J. Lepak and M. Crescimanno, *Speed of light measurement using ping*, (2002), SAO/NASA ADS: http://adsabs.harvard.edu/abs/2002physics...1053L arXiv: http://arxiv.org/abs/physics/0201053.

[30] J.W. Moore, *Meteorology practical and applied*, Rebman limited, 1910, Image from: http://commons.wikimedia.org/wiki/File:Gold_leaf_electroscope_with_ground_strips.png.

[31] P. Moreira, J. Serrano, T. Wlostowski, P. Loschmidt, and G. Gaderer, *White Rabbit: Sub-Nanosecond Timing Distribution over Ethernet*, ISPCS (International Symposium on Precision Clock Synchronization for Measurement, Control and Communication), IEEE, 2009, pp. 1–5.

[32] User:Mpfiz, *AirShower.svg*, 2008, Wikimedia Commons, a free media database. http://commons.wikimedia.org/wiki/File:AirShower.svg.

[33] D. Pacini, *La radiazione penetrante alla superficie ed in seno alle acque*, Il Nuovo Cimento **VI/III** (1912), 93–100.

[34] D. Pacini, *Penetrating Radiation at the Surface of and in Water*, (2010), translated and commented by Alessandro De Angelis SAO/NASA ADS: http://adsabs.harvard.edu/abs/2010arXiv1002.1810P arXiv: http://arxiv.org/abs/1002.1810.

[35] Pierre Auger Collaboration and et al., *Correlation of the Highest-Energy Cosmic Rays with Nearby Extragalactic Objects*, Science **318** (2007), 938, SAO/NASA ADS: http://adsabs.harvard.edu/abs/2007Sci...318..938P

arXiv: http://arxiv.org/abs/0711.2256.

[36] ———, *The Fluorescence Detector of the Pierre Auger Observatory*, ArXiv e-prints (2009),
SAO/NASA ADS: http://adsabs.harvard.edu/abs/2009arXiv0907.4282T
arXiv: http://arxiv.org/abs/0907.4282.

[37] Nils Pipenbrink, *asyncwriter*, 2012, unpublished software.

[38] J. Ranft and W. R. Nelson, *Hadron cascades induced by electron and photon beams in the GeV energy range*, Tech. Report SLAC-PUB-3959, SLAC, May 1986,
CERN Document Server: http://cdsweb.cern.ch/record/173506/
SLAC Scientific Documents: http://www-public.slac.stanford.edu/sciDoc/docMeta.aspx?slacPubNumber=SLAC-PUB-3959.

[39] Stefan Ritt, *DRS Chip Documentation*, http://drs.web.psi.ch/evaluation/.

[40] ———, *Design and Performance of the 6 GS/s Waveform Digitizing Chip DRS4*, conference talk at the IEEE Nuclear Science Symposium (NSS), 2008, also published on http://drs.web.psi.ch.

[41] ———, *9 Channel, 5 GSPS Switched Capacity Array DRS4*, preliminary datasheet (revision 0.9), July 2009, published on http://drs.web.psi.ch.

[42] ———, *DRS4 Evaluation Board User's Manual (Board Revision 3.1)*, February 2011, published on http://drs.web.psi.ch.

[43] F. G. Schröder, T. Asch, L. Bähren, J. Blümer, H. Bozdog, H. Falcke, A. Haungs, A. Horneffer, T. Huege, P. G. Isar, O. Krömer, and S. Nehls, *New method for the time calibration of an interferometric radio antenna array*, Nuclear Instruments and Methods in Physics Research A **615** (2010), 277–284,
SAO/NASA ADS: http://adsabs.harvard.edu/abs/2010NIMPA.615..277S
arXiv: http://arxiv.org/abs/1002.3775.

[44] D. Sobczynska, *Natural limit on the gamma/hadron separation for a stand alone air Cherenkov telescope*, Journal of Physics G Nuclear Physics **34** (2007), 2279–2288,
SAO/NASA ADS: http://adsabs.harvard.edu/abs/2007JPhG...34.2279S
arXiv: http://arxiv.org/abs/astro-ph/0702562.

[45] M. Tluczykont and et al., *The HiSCORE experiment and its potential for gamma-ray astronomy*, 23rd European Cosmic Ray Symposium, Moscow, 2012.

[46] M. Tluczykont, D. Hampf, D. Horns, T. Kneiske, R. Eichler, R. Nachtigall, and G. Rowell, *The ground-based large-area wide-angle γ-ray and cosmic-ray experiment HiSCORE*, Advances in Space Research **48** (2011), 1935–1941,
SAO/NASA ADS: http://adsabs.harvard.edu/abs/2011AdSpR..48.1935T
arXiv: http://arxiv.org/abs/1108.5880.

[47] H. Ulrich, *Untersuchungen zum primären Energiespektrum der kosmischen Strahlung im PeV-Bereich mit dem KASCADE-Experiment*, Forschungszentrum Karlsruhe: Wissenschaftliche Berichte, vol. FZKA 6952, Forschungszentrum Karlsruhe, 2004.

[48] Pavel Vyskočil and Jiří Šebesta, *Relative Timing Characteristics of GPS Timing Modules for Time Synchronization Application*, International Workshop on Satellite and Space Communications 2009, 2009, pp. 230–234.

[49] Ralf Wischnewski and Martin Brückner, *Time Synchronization and Array Trigger in CTA with WhiteRabbit: Ready to go . . .*, talk at the CTA Collaboration Meeting in Rome (Italy), October 2012, also published on `http://www.ifh.de/~wischnew/talks/cta/collaboration_rome_201210/`.

[50] T. Wulf, *Über die in der Atmosphäre vorhandene Strahlung von hoher Durchdringungsfähigkeit*, Physikalische Zeitschrift **V** (1909), 152–157.

[51] G. T. Zatsepin and V. A. Kuzmin, *Upper Limit of the Spectrum of Cosmic Rays*, Soviet Journal of Experimental and Theoretical Physics Letters **4** (1966), 78, SAO/NASA ADS: `http://adsabs.harvard.edu/abs/1966JETPL...4...78Z`.

B. Source code

B.1. drs_speedtest.cpp

```
1  #include <stdio.h>
2  #include <stdlib.h>
3  #include <stdint.h>
4  #include <string.h>
5  #include <sys/time.h>

7  #include "DRS.h"
8  #include "asyncwriter.h"

10 #define FRAMESIZE 16408
11 #define HEADERSIZE 4100
12 #define EVTSPERFILE 6000

14 // calculate the difference between two timestamps.
15 void timeval_subtract(struct timeval *result, struct timeval *t2,
                         struct timeval *t1) {
16   long int diff = (t2->tv_usec+1000000 * t2->tv_sec) -
                     (t1->tv_usec+1000000 * t1->tv_sec);
17   result->tv_sec = diff / 1000000;
18   result->tv_usec = diff % 1000000; }

20 // give a filename as a const char* incorporating the given number
21 const char* filename(int fnum) {
22   static char strbuf[30];
23   sprintf(strbuf, "speedtest_data_%05i.dat", fnum);
24   return strbuf; }

26 int main(int argc, char *argv[])
27 {
28   int maxevts, fcount = 0; // run control vars
29   bool usef;

31   DRS *drs; // device control vars
32   DRSBoard *b;
33   float time_array[1024];
34   float wave_array[4][1024];
35   float t, d; // output control/encoding vars
36   unsigned char timeheader[HEADERSIZE];
37   unsigned char buffer[FRAMESIZE];
38   unsigned char *p;
39   AsyncWriter asyncFile(4, 4, FRAMESIZE);

41   struct timeval tvBegin, tvEnd, tvDiff; //timing vars
42   float diffsecs;

44   // read the command line arguments and try to figure out what
                the user wants
45   const char* usage = "Usage: drs_speedtest <maxevts>
                [nofile]\n <maxevts>: Number of events to be
                collected\n [nofile]: Provide an arbitrary third
                argument to prevent file writeout\n";
46   if ( argc == 2 or argc == 3 ) {
47     maxevts = atoi(argv[1]);
48     if (maxevts == 0) { printf("%s",usage); return 1; }
49     switch ( argc ) {
```

```
50        case 2: printf("Collecting and saving %i events ...\n",
                      maxevts); usef = true; break;
51        case 3: printf("Collecting %i events without saving ...\n",
                      maxevts); usef = false; break;
52      }
53    }
54    else { printf("%s",usage); return 1; }

56    // initialize the DRS board
57    drs = new DRS();
58    if (drs->GetNumberOfBoards() == 0) return 1;
59    b = drs->GetBoard(0);
60    b->Init();
61    b->SetFrequency(1, true);
62    b->SetInputRange(0); //0 for -0.5--0.5 or 0.5 for 0--1
63    b->EnableTrigger(1, 0); // lemo on/off, channel trigger on/off
64    b->SetTriggerDelayNs(0); // zero ns trigger delay

66    // start timing (connection setup is excluded)
67    gettimeofday(&tvBegin, NULL);

69    // read out the time array (just once, because it changes only
70    // on re-calibration), then write it to the data file as 'header'
71    b->GetTime(0, b->GetTriggerCell(0), time_array);
72    if (usef) {
73      p = timeheader;
74      memcpy(p, "THDR", 4);
75      p += 4;
76      for (int i=0 ; i<1024 ; i++) {
77        t = time_array[i];
78        *(float *)p = t;
79        p += 4;
80      }
81      asyncFile.openFile(filename(fcount++), timeheader,
                      HEADERSIZE);
82    }

84    // main loop: read weaves and save them
85    static int j=0;
86    while (j<maxevts) {
87      b->StartDomino();
88      while (b->IsBusy());
89      b->TransferWaves(0, 8);
90      b->GetWave(0, 0, wave_array[0]);
91      b->GetWave(0, 2, wave_array[1]);
92      b->GetWave(0, 4, wave_array[2]);
93      b->GetWave(0, 6, wave_array[3]);

95      if ( usef ) {
96        p = buffer;
97        memcpy(p, "EHDR", 4);
98        p += 4;
99        *(uint32_t *)p = j;
100       p += 4;
101       for (int ch=1 ; ch<=4 ; ch++) {
102         sprintf((char *)p, "C%03d", ch);
103         p += 4;
104         for (int i=0 ; i<1024 ; i++) {
105           d = wave_array[ch-1][i];
106           *(float *)p = d;
107           p += 4;
108         }
109       }
110       asyncFile.writeFile(buffer);

112       // open a new file with a higher number if a wrap is in order
113       // every new file gets the time array as header
```

```
114       if (j>0 and (j+1)<maxevts and (j+1)%EVTSPERFILE ==
                      0) {
115         asyncFile.closeFile();
116         asyncFile.openFile(filename(fcount++), timeheader,
                        HEADERSIZE);
117       }
118     }
119     j++;
120   }

122   // stop timing and calculate the frequency
123   gettimeofday(&tvEnd, NULL);
124   timeval_subtract(&tvDiff, &tvEnd, &tvBegin);
125   diffsecs = float(tvDiff.tv_sec)+float(tvDiff.tv_usec)/1000000;

127   // close the file
128   if ( usef ) {
129     asyncFile.closeFile();
130     printf("Read %i events into %i file(s) in %.4f seconds.
                      Frequency: %.2lf Hz\n", j, fcount, diffsecs,
                      float(j)/diffsecs);
131   } else {
132     printf("Read %i events in %.4f seconds. Frequency: %.2lf
                      Hz\n", j, diffsecs, float(j)/diffsecs); }

134   //close usb connection
135   delete drs;
136 }
```

B.2. drs_speedtest_binexplode.py

```
import os, sys
import struct
HSIZE = 4100
FSIZE = 16408

dirlist = os.listdir(os.curdir)
extlist = [e[1] for e in [os.path.splitext(f) for f in dirlist]]
if extlist.count('.dat') == 1:
  infilename = dirlist[extlist.index('.dat')]
else:
  if len(sys.argv) >= 2:
    if os.path.isfile(sys.argv[1]):
      infilename = sys.argv[1]
    else:
      print "There is not exactly one .dat file, and the specified
                    file doesn't exist. Exiting."
      raise SystemExit
  else:
    print "There is not exactly one .dat file, and no file is
                  specified. Exiting."
    raise SystemExit

print "Using %s" % infilename
infile = open(infilename,'rb')

# how many events are there?
infile.seek(0,2)
infilesize = infile.tell()
eventnumber = (infilesize - HSIZE) / FSIZE
print "%i events in this file."%eventnumber
infile.seek(HSIZE,0)
(offset,) = struct.unpack('4xI',infile.read(2*4))
infile.seek(0,0)

times = struct.unpack('4x1024f',infile.read(HSIZE))

while infile.tell() < infilesize:
  outfilelines = ["TIME CH1 CH2 CH3 CH4\n"]

  (eventindex,) = struct.unpack('4xI',infile.read(2*4))
  eventcount = eventindex-offset
  if (eventcount+1) % (eventnumber/10) == 0:
    print "%05i of %i ..." % (eventcount+1, eventnumber)

  ch1 = struct.unpack('4x1024f',infile.read(1025*4))
  ch2 = struct.unpack('4x1024f',infile.read(1025*4))
  ch3 = struct.unpack('4x1024f',infile.read(1025*4))
  ch4 = struct.unpack('4x1024f',infile.read(1025*4))

  data = [ [ "%.1f"%vals[i] for vals in [times,ch1,ch2,ch3,ch4] ]
                for i in range(1024) ]
  outfilelines = [ ' '.join(L)+'\n' for L in data ]

  outfilepath = '%05i' % (eventcount+1)
  outfile = open(outfilepath,'w')
  outfile.writelines(outfilelines)
  outfile.close()
```

B.3. Clock timestamp fitting

```
from __future__ import division
import os,sys,re
from numpy import *
from scipy import optimize

carrfrq = 5. #frequency in MHz
carrier = 1e3/(carrfrq) #period in ns

# calibration data
# [min/2,max/2] of modulated signal's peak-to-peak amplitude
cal1 = [32.3/2,903.9/2] # setup 1
cal2 = [147.3/2,984.3/2] # setup 2

cal = cal1 # current data set

def fit(X,y,rps,carrier,cal):
    roughamp = (max(y)-min(y))/2
    fitfunc = lambda p,x: p[2]+p[0]*sin(2*pi/carrier*x+p[1])
    errfunc = lambda p,x,y: fitfunc(p,x)-y
    pfit = [roughamp,0,0]
    pres,success = optimize.leastsq(errfunc,pfit,args=(asarray(X),y))
    fittime = (abs(pres[0])-cal[0])/(cal[1]-cal[0])*1000
    print "%s: Long ramp amplitude %.1f corresponds to %.1f%s,
                oscilloscope should read %.1fms." % \
        (infile, abs(pres[0]), fittime, {1000:'us',1:'ms'}[rps],
                -1000.0+fittime)
    print infile, "%s fit parameters: [amp,phase,offset]",pres

def backcal(osctime,cal):
    return (1000-osctime)*(cal[1]-cal[0])/1000+cal[0]

#find files
infiles = []
for indirfile in os.listdir(os.curdir):
    if re.match('^\d{5}$',indirfile): infiles.append(indirfile)
if not infiles: raise SystemExit

for infile in infiles:
    #read in and prep the numbers from the file
    infilehandle = open(infile,'r')
    inlines = [l.strip().split(' ') for l in infilehandle.readlines()[1:]]
    infilehandle.close()
    # throw away the first 4 and the last 2 values,
    # because they are often erroneous outliers
    X = [ float(j.replace(',','.')) for j in [i[0] for i in inlines] ][4:-1]
    y1 = [ float(j.replace(',','.')) for j in [i[1] for i in inlines] ][4:-1]
    y2 = [ float(j.replace(',','.')) for j in [i[2] for i in inlines] ][4:-1]
    # do the fit
    fit(X,y1,1,carrier,cal1)
```

C. Data tables

C.1. `drs_speedtest.cpp` data structure

The table below is a schematic representation of the bytewise data structure of a data file produced by `drs_speedtest`. ASCII headers allow for consistency checking and manual orientation within the file at an overhead of $\sim 0.1\,\%$.

quantity	data type	bytes	byte position first	byte position last	function
4	`char`	4	0	3	ASCII: "`THDR`" (time header)
1024	`float`	4096	4	4099	Time calibration data
4	`char`	4	4100	4103	ASCII: "`EHDR`" (event header)
1	`long int`	4	4104	4107	Event serial number
4	`char`	4	4108	4111	ASCII: "`C001`" (Channel header)
1024	`float`	4096	4112	8207	Cell data
4	`char`	4	8208	8211	ASCII: "`C002`"
1024	`float`	4096	8212	12307	Cell data
4	`char`	4	12308	12311	ASCII: "`C003`"
1024	`float`	4096	12312	16407	Cell data
4	`char`	4	16408	16411	ASCII: "`C004`"
1024	`float`	4096	16412	20507	Cell data
4	`char`	4	20508	20511	ASCII: "`EHDR`"
1	`long int`	4	20512	20515	Event serial number
4	`char`	4	20516	20519	ASCII: "`C001`"
1024	`float`	4096	20520	24615	Cell data
4	`char`	4	24616	24619	ASCII: "`C002`"
1024	`float`	4096	24620	28715	Cell data
4	`char`	4	28716	28719	ASCII: "`C003`"
1024	`float`	4096	28720	32815	Cell data
4	`char`	4	32816	32819	ASCII: "`C004`"
1024	`float`	4096	32820	36915	Cell data
4	`char`	4	36916	36919	ASCII: "`EHDR`"
1	`long int`	4	36920	36923	Event serial number
⋮					

C.2. Extensive air shower composition

Simulated primary particle energy: $5 \cdot 10^{14}$ eV. Image and simulation from [16, p. 28].

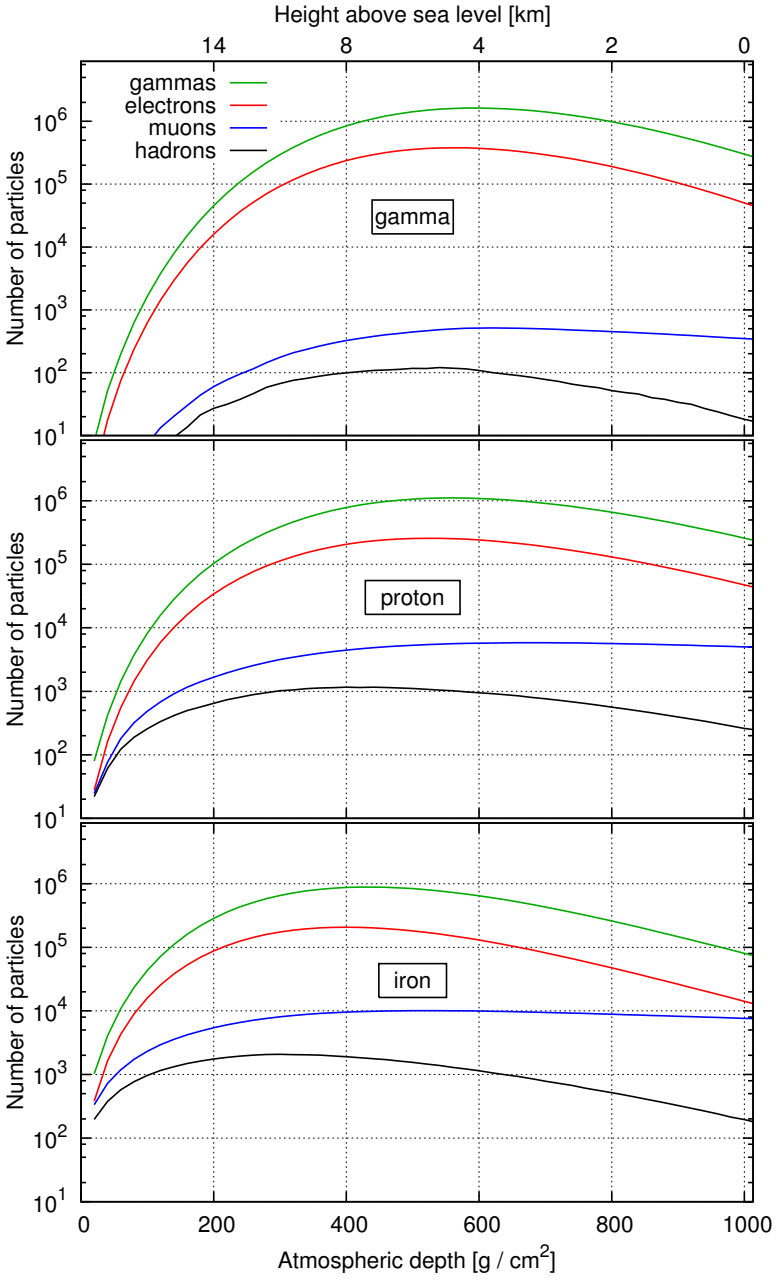

D. Formal and personal statements

D.1. Erklärung nach § 21 (9) DiplPrüfO v. 9. Juni 2003

Ich erkläre hiermit, dass ich die vorliegende Diplomarbeit selbstständig verfasst und nur die angegebenen Quellen und Hilfsmittel benutzt habe.

Weiterhin bin ich mit einer Veröffentlichung dieser Arbeit einverstanden.

Hamburg, den Michael Büker

D.2. Acknowledgements/Danksagung

In the name of the H$_i$SCORE collaboration, I would like to thank for their special contributions to this work (in alphabetical order):

Peter Göttlicher of the Electronics Development Group of DESY in Hamburg for taking the time to provide valuable insight on the feasibility and challenges of an implementation of the Clock proposed in this work.

Nils Pipenbrink from Hamburg for preparing and providing his `asyncwriter` software, which provides an important part of the functionality of the `drs_speedtest` software presented in this work.

Stefan Ritt of the Paul Scherrer Institute in Villigen (Switzerland) for enabling me to visit PSI, patiently dedicating time to me and my questions and providing me with vital insight on the workings and development of the DRS chip.

Synergy Systems, LLC of San Diego, California (USA) for the generous donation of their SynTAC GPS readout and control software.

Any attempt to mention all those who have personally helped and supported me in my work would probably be lengthy and yet incomplete. I have received inspiration, advice, counsel and assistance from many wonderful people without whom I would never have come this far. To my teachers, fellow students and scientific colleagues, to my friends, my Twitter timeline, my family and the people close to me—I am deeply grateful to you.

Jeder Versuch, all diejenigen zu erwähnen, die mir persönlich in meiner Arbeit Hilfe geleistet und mich unterstützt haben, wäre wahrscheinlich langwierig und doch unvollständig. Ich habe von vielen tollen Menschen Eingebung, Rat, Hilfe und Unterstützung erhalten, ohne die ich nie so weit gekommen wäre. Meinen Lehrenden, Kommilitonen und wissenschaftlichen Kollegen, meinen Freunden, meiner Twitter-Timeline, meiner Familie und den Menschen, die mir nahestehen – Euch gebührt mein tiefer Dank.